ARMY RESEARCH LABORATORY

Lateral Control Jet Aerodynamic Predictions for a 2.75-in Rocket Testbed Munition

by Paul Weinacht

ARL-TR-3165 **April 2004**

NOTICES

Disclaimers

The findings in this report are not to be construed as an official Department of the Army position unless so designated by other authorized documents.

Citation of manufacturer's or trade names does not constitute an official endorsement or approval of the use thereof.

Destroy this report when it is no longer needed. Do not return it to the originator.

Army Research Laboratory
Aberdeen Proving Ground, MD 21005-5066

ARL-TR-3165 **April 2004**

Lateral Control Jet Aerodynamic Predictions for a 2.75-in Rocket Testbed Munition

Paul Weinacht
Weapons and Materials Research Directorate, ARL

Report Documentation Page

Form Approved
OMB No. 0704-0188

1. REPORT DATE *(DD-MM-YYYY)*	2. REPORT TYPE	3. DATES COVERED (From - To)
April 2004	Final	2001–2003

4. TITLE AND SUBTITLE
Lateral Control Jet Aerodynamic Predictions for a 2.75-in Rocket Testbed Munition

5a. CONTRACT NUMBER

5b. GRANT NUMBER

5c. PROGRAM ELEMENT NUMBER

6. AUTHOR(S)
Paul Weinacht

5d. PROJECT NUMBER
1L1612618AH80

5e. TASK NUMBER

5f. WORK UNIT NUMBER

7. PERFORMING ORGANIZATION NAME(S) AND ADDRESS(ES)
U.S. Army Research Laboratory
ATTN: AMSRD-ARL-WM-BC
Aberdeen Proving Ground, MD 21005-5066

8. PERFORMING ORGANIZATION REPORT NUMBER
ARL-TR-3165

9. SPONSORING/MONITORING AGENCY NAME(S) AND ADDRESS(ES)

10. SPONSOR/MONITOR'S ACRONYM(S)

11. SPONSOR/MONITOR'S REPORT NUMBER(S)

12. DISTRIBUTION/AVAILABILITY STATEMENT
Approved for public release; distribution is unlimited.

13. SUPPLEMENTARY NOTES

14. ABSTRACT
The aerodynamic performance of lateral control jets for a 2.75-in rocket testbed munition has been investigated using a sophisticated numerical technique. The computational approach utilized a finite difference-based overset gridding approach to predict the interaction of the lateral control jet with the external flow around the munition and the resulting effect on the lateral control jet performance. The jet interaction effect was found to be an important contributor to the overall effectiveness of the lateral control jet. The circumferential location of the jet relative to the tail fins was also found to influence the jet's effectiveness. A variation of 30% in the net jet moment was computed for the two fin orientations considered in the study. The predictions also showed that spin did not significantly influence the lateral control jet performance for the expected spin rates of the testbed munition; however, if the spin was increased significantly, the resulting jet interaction produced a misalignment of the total jet thrust relative to the nozzle. Single and tandem jet configurations were examined. For the configurations examined here, the tandem jet doubled the effective jet thrust, although a similar effective jet thrust could be obtained by sequential independent firings of both jets. Time-dependent predictions of the performance of pulsed lateral control jets indicate that steady-state flow is attained during the duration of the firing cycle, and the overall performance of the pulsed jets can be represented reasonably well by the steady-state jet-on performance.

15. SUBJECT TERMS
aerodynamics, projectile flight mechanics, lateral control jets

16. SECURITY CLASSIFICATION OF:			17. LIMITATION OF ABSTRACT	18. NUMBER OF PAGES	19a. NAME OF RESPONSIBLE PERSON
a. REPORT	b. ABSTRACT	c. THIS PAGE			Paul Weinacht
UNCLASSIFIED	UNCLASSIFIED	UNCLASSIFIED	UL	40	19b. TELEPHONE NUMBER (*Include area code*) 410-278-4280

Standard Form 298 (Rev. 8/98)
Prescribed by ANSI Std. Z39.18

Contents

List of Figures

List of Tables

Acknowledgments

This work was supported by a grant of computer time from the Department of Defense High Performance Computing Major Shared Resource Center at the U.S. Army Research Laboratory.

INTENTIONALLY LEFT BLANK.

1. Introduction

The U.S. Army Research Laboratory is currently investigating smart munition technologies as a means of improving the lethality and accuracy of future generations of munitions. One of the focuses of the current effort is the development of integrated multidisciplinary design technologies such as structural dynamics, computational fluid dynamics (CFD), and guidance, navigation and control. These multidisciplinary design technologies allow complex munitions systems to be studied and visualized within high-performance computational environments to determine the nonlinear interaction of critical engineering parameters using high-fidelity physics. Detailed design trades can be performed on system subcomponents, enabling the optimization of the munitions system as a whole. Critical structural and functional shortcomings in the system/subsystems (such as embedded devices/electronics) can be identified and the system can be redesigned before any hardware is manufactured, resulting in reduced development costs and higher performance munitions.

As part of this effort, a 2.75-in rocket has been modified as a testbed for investigating the in-flight response of a flight vehicle subjected to lateral control jets (*1*). The testbed vehicle, shown in figure 1, incorporates numerous modifications including several lateral control jets/thrusters in the forward portion of the body, instrumentation to control, measure, and telemeter the vehicle flight dynamic response, and a specially designed composite body section with embedded strain gauges to measure the structural response. To support the experimental program, CFD has been performed to assess the aerodynamic performance of the lateral control jets. The results of these studies are detailed in the current report.

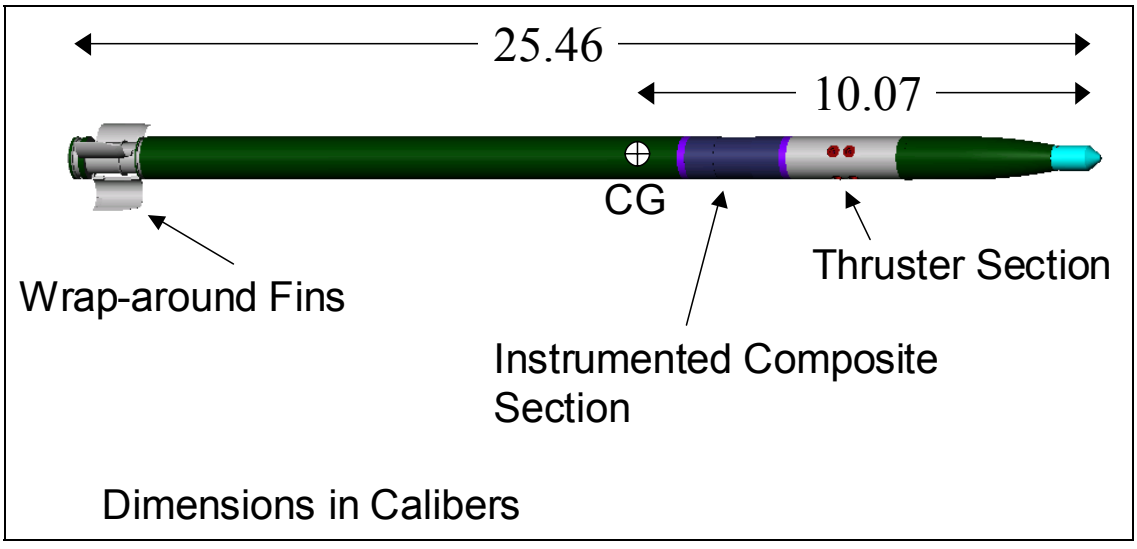

Figure 1. Schematic of 2.75-in rocket testbed vehicle.

The CFD capability applied here for the lateral control jet problem has been validated in previous studies (*2*, *3*). In these studies, detailed comparisons of the computed surface pressure distribution was made with wind tunnel measurements. The focus of the CFD effort was the prediction of the aerodynamic performance of lateral control jets on the testbed munition. As part of this effort, time-dependent aerodynamic loads produced by the lateral control jet firings were also determined. Lateral control jets provide a convenient means of providing control authority for a flight vehicle because the external aerodynamics are unaffected except during the controlled portion of the flight. However, the flow field that results from the interaction between the gaseous jet and the external flow is complicated and can modify the overall effectiveness of the lateral control jet.

Figure 2 shows a schematic representation of the flow field produced by a lateral control jet in supersonic flight. The qualitative features of the jet-interaction flow field include regions of shock/boundary-layer interaction and flow separation that have an effect on the large regions of the flow field around the body. The jet creates a blocking effect to the oncoming flow in the vicinity of the nozzle, producing boundary-layer separation and recirculation upstream of the jet. The separation region upstream of the jet sets up a wedge-shaped area, which has the effect of deflecting the flow laterally around the body so that a region of high pressure is felt under the projectile. The details of the upstream interaction are important because it is along the upper part of this region that the separation shock forms.

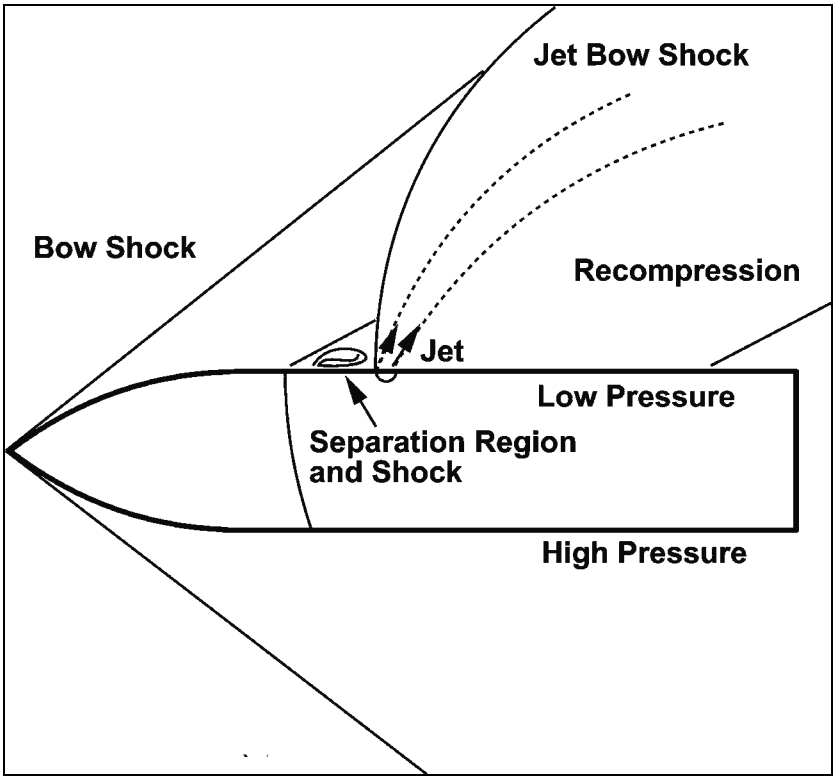

Figure 2. Schematic of jet-interaction flow field.

Since the jet stream acts as an obstacle to the external flow, another shock wave originates directly upstream of the jet and above the separation region called the jet bow shock. The jet-bow shock moves outward from the body and bends backward as the jet flow is deflected by the external flow. A strong turbulent wake results from the jet flow field interactions and extends over a significant portion of the projectile body. Eventually, a recompression shock forms in the wake downstream of the jet. The jet-bow shock also moves laterally around the jet, the effects of which are felt on the underbody of the projectile. If there are tail fins present, the wake behind the jet can also interact with these control surfaces resulting in additional changes to the jet effectiveness.

For the jet-interaction problem, the total force acting on the body can be separated into the following three components: (1) the aerodynamic force on the external body in the absence of the jet, (2) the force produced by the jet thrust, and (3) the aerodynamic-interaction force produced by the jet with the external flow field. In the current paper, all computations have been performed at 0° angle of attack and the transverse aerodynamic force on the external body is 0. The jet thrust results from a combination of the momentum flux through the jet nozzle and the integrated pressure at the jet exit and over the nozzle surface. The third force component accounts for the force produced by the interaction of the jet with the external flow field.

The relationship of these three force components to the total lateral force, F, can be described by the following equation, where $F_{no\text{-}jet}$ is the force in the absence of the jet, F_j is the force produced at the jet exit, and F_{ji} is the jet interaction force:

$$F = F_{no-jet} - \left(F_j + F_{ji}\right). \tag{1}$$

The negative sign associated with the two jet forces results because the jet nozzle is located on the upper surface of the body in the current study and produces a downward force when activated. The jet-off force component typically produces an upward force for positive angles of attack. Note that a positive value of F_{ji} indicates that the interaction force produces an effect that augments the jet force F_j, while a negative value of F_{ji} indicates a reduction in the total force produced by the jet. The jet-interaction force accounts for the complete interaction produced by the jet with the external flow field and may vary with angle of attack and jet mass flow rate.

The relative magnitudes of the jet force and the jet interaction force can be compared through a jet interaction force amplification factor, K, as shown in equation 2.

$$K = \frac{F_j + F_{ji}}{F_j}. \tag{2}$$

An amplification factor >1 indicates that the jet interaction force amplifies or increases the total force produced by the jet, while an amplification factor <1 indicates that the jet interaction force reduces the total force produced by the jet. Similarly, a jet interaction moment amplification

factor can be defined where M_j and M_{ji} are the moment produced by the jet thrust and the jet interaction moment, respectively (*3*).

$$K_m = \frac{M_j + M_{ji}}{M_j}. \tag{3}$$

For short-duration jets which effectively produce linear and angular impulses to the body rather than steady-state forces or moments, a jet interaction impulse amplification factor can be defined in a manner analogous to the force and moment amplification factors, I and I_m.

$$I = \frac{\int_0^\infty F_j dt + \int_0^\infty F_{ji} dt}{\int_0^\infty F_j dt}. \tag{4}$$

$$I_m = \frac{\int_0^\infty M_j dt + \int_0^\infty M_{ji} dt}{\int_0^\infty M_j dt}. \tag{5}$$

In the current study, the CFD approach was applied to assess the aerodynamic performance of the lateral control jets on the testbed munition. The jet thrust, jet-interaction force and moments, and jet-interaction amplification factors have been determined for the testbed munition. Single and simultaneous dual-jet firings have been examined. The role of fin orientation relative to the jet for these asymmetrical fins has also been considered. Additionally, the effect of body-roll rate on the aerodynamic performance of the jets has been predicted. Finally, both the steady-state and short-duration time-dependent response of the lateral control jet have been assessed and compared.

Comparisons of the global forces and moment produced by the jet interaction flow field were also made. The validation has been conducted for axisymmetric bodies and bodies with strakes and tail fins. A brief description of the computational approach applied this study is provided in the following section.

2. Computational Approach

The nonreacting compressible Newtonian viscous flow about a flight vehicle is governed by the equations of mass, momentum, and energy conservation—the Navier-Stokes equations. For these computations, the complete set of three-dimensional, time-dependent, generalized-geometry, Reynolds-averaged, thin-layer, Navier-Stokes equations for generalized coordinates ξ, η, and ζ are used and can be written as follows (*4*):

$$\frac{\partial \hat{q}}{\partial t}+\frac{\partial \hat{E}}{\partial \xi}+\frac{\partial \hat{F}}{\partial \eta}+\frac{\partial \hat{G}}{\partial \zeta}+\hat{H}=\frac{1}{Re}\frac{\partial \hat{S}}{\partial \zeta}, \tag{6}$$

where $\xi=\xi(x,y,z,t)$, $\eta=\eta(x,y,z,t)$, and $\zeta=\zeta(x,y,z,t)$ are the longitudinal coordinate (direction along the body), the circumferential coordinate (direction around the body), and the nearly-normal coordinate (outward direction from the body surface), respectively.

The inviscid-flux vectors, $\hat{E}$, $\hat{F}$, and $\hat{G}$, and the viscous term $\hat{S}$ are functions of the dependent variable, $\hat{q}^T=(\rho,\rho u,\rho v,\rho w,e)/J$. The source term, $\hat{H}$, incorporates the effects of the centrifugal and Coriolis forces from the rotating-coordinate frame produced by rolling motion. The inviscid-flux vectors and the source term are shown below. Details of the thin-layer viscous term are available in the literature.

$$\hat{E}=\frac{1}{J}\begin{bmatrix}\rho U\\ \rho uU+\xi_x p\\ \rho vU+\xi_y p\\ \rho wU+\xi_z p\\ (e+p)U\end{bmatrix}\quad \hat{F}=\frac{1}{J}\begin{bmatrix}\rho V\\ \rho uV+\eta_x p\\ \rho vV+\eta_y p\\ \rho wV+\eta_z p\\ (e+p)V\end{bmatrix}$$

$$\hat{G}=\frac{1}{J}\begin{bmatrix}\rho W\\ \rho uW+\zeta_x p\\ \rho vW+\zeta_y p\\ \rho wW+\zeta_z p\\ (e+p)W\end{bmatrix}\quad \hat{H}=\frac{1}{J}\begin{bmatrix}0\\ \rho f_x\\ \rho f_y\\ \rho f_z\\ \rho u f_x+\rho v f_y+\rho w f_z\end{bmatrix}, \tag{7}$$

where

$$\begin{aligned}U&=u\xi_x+v\xi_y+w\xi_z\\ V&=u\eta_x+v\eta_y+w\eta_z\\ W&=u\zeta_x+v\zeta_y+w\zeta_z\end{aligned} \tag{8}$$

$$\begin{aligned}&\xi_x=J(y_\eta z_\zeta-z_\eta y_\zeta) \quad \xi_y=J(z_\eta x_\zeta-x_\eta z_\zeta)\\ &\xi_z=J(x_\eta y_\zeta-y_\eta x_\zeta) \quad \eta_x=J(y_\zeta z_\xi-z_\zeta y_\xi)\\ &\eta_y=J(z_\zeta x_\xi-x_\zeta z_\xi) \quad \eta_z=J(x_\zeta y_\xi-y_\zeta x_\xi)\\ &\zeta_x=J(z_\eta y_\xi-y_\eta z_\xi) \quad \zeta_y=J(x_\eta z_\xi-z_\eta x_\xi)\\ &\zeta_z=J(y_\eta x_\xi-x_\eta y_\xi)\\ &J=1/[x_\xi(y_\eta z_\zeta-y_\zeta z_\eta)+x_\eta(y_\xi z_\zeta-y_\zeta z_\xi)+x_\zeta(y_\xi z_\eta-y_\eta z_\xi)].\end{aligned} \tag{9}$$

The pressure, p, can be related to the dependent variables by applying the ideal gas law.

$$p = (\gamma - 1)\left[e - \frac{\rho}{2}\left(u^2 + v^2 + w^2\right)\right]. \tag{10}$$

The form of the mass-averaged Navier-Stokes equations requires a model for the turbulent eddy viscosity. There are numerous approaches for determining the turbulent viscosity. The turbulent contributions are supplied through the algebraic two-layer eddy viscosity model developed by Baldwin and Lomax (*5*), which is patterned after the model of Cebeci (*6*).

The Coriolis and centrifugal acceleration terms due to the rotating coordinate system which are contained in the source term, $\hat{H}$, are shown in the following:

$$\vec{f} = 2\vec{\Omega} \times \vec{u} + \vec{\Omega} \times \left(\vec{\Omega} \times \vec{R}\right). \tag{11}$$

The Coriolis acceleration is a function of the angular velocity of the coordinate frame with respect to the inertial frame, $\vec{\Omega}$, and the fluid velocity vector, $\vec{u}$, which can be represented by the velocity components, u, v, and w. The centripetal acceleration is a function of the angular velocity of the rotating frame, $\vec{\Omega}$, and the displacement vector, $\vec{R}$, between the axis of rotation and the particular location in the flow field. The acceleration vector, $\vec{f}$, can be written in terms of its components along the x, y, and z axes, f_x, f_y, and f_z. The angular velocity of the rotating coordinate frame due to pure rolling motion is written as follows:

$$\vec{\Omega} = \Omega \vec{i}_x . \tag{12}$$

For the case of rolling motion, the source term takes the following form:

$$\hat{H}^T = \frac{1}{J}\left[0, H_2, H_3, H_4, H_5\right], \tag{13}$$

where

$$\begin{aligned} H_2 &= 0 \\ H_3 &= -2\Omega\rho w - \rho\Omega^2 y \\ H_4 &= 2\Omega\rho v - \rho\Omega^2 z \\ H_5 &= -\Omega^2\left(y\rho v + z\rho w\right). \end{aligned} \tag{14}$$

2.1 Numerical Technique

The time-dependent Navier-Stokes equations are solved using a time-iterative solution technique to obtain the final steady-state converged solution. The particular time-marching technique applied here is the implicit, partially flux-split, upwind numerical scheme developed by Ying et al. (*7*) and Sahu and Steger (*8*), and is based on the flux-splitting approach of Steger and Warming (*9*). In its original form, the technique was referred to as the F3D technique. This scheme utilizes central differencing in the normal and circumferential directions, η and ζ, respectively, and flux splitting in the streamwise direction, ξ. Rather than directly invert the

implicit equation, a two-factor implicit technique similar to that of Steger and Buning (*10*) is utilized. The resulting factored implicit equation is shown as follows:

$$\left[I + i_b h \delta_\xi^b \left(\hat{A}^+ \right)^n + i_b h \delta_\zeta \hat{C}^n + i_b h \hat{D}^n - i_b h \frac{1}{Re} \bar{\delta}_\zeta \frac{1}{J} \hat{M}^n J - i_b D_i \,|_\zeta \right] q^* = RHS, \qquad (15)$$

$$\left[I + i_b h \delta_\xi^f \left(\hat{A}^- \right)^n + i_b h \delta_\eta \hat{B}^n - i_b D_i \,|_\eta \right] \Delta \hat{q}^n = q^*, \qquad (16)$$

and

$$RHS = -i_b \Delta t \left(\delta_\xi^b \left(\hat{E}^+ \right)^n + \delta_\xi^f \left(\hat{E}^- \right)^n + \delta_\eta \hat{F}^n + \delta_\zeta \hat{G}^n + \hat{H}^n - \frac{1}{Re} \bar{\delta} \hat{S}^n - D_e \hat{q}^n \right), \qquad (17)$$

where $h = \Delta t$. Here, δ is typically a three-point, second-order accurate central difference operator, $\bar{\delta}$ is a midpoint operator used with the viscous terms, and the operators δ_ζ^f and δ_ζ^b are the forward and backward, respectively, three-point difference operators. The Jacobian matrices $\hat{A}$, $\hat{B}$, $\hat{C}$, $\hat{D}$, and $\hat{M}$ result from local linearization of the fluxes about the previous time level (*11*) (e.g., $\hat{E}^{n+1} = \hat{E}^n + \hat{A}^n \left(\hat{q}^{n+1} - \hat{q}^n \right) + O\left(\Delta t^2 \right)$, where $\hat{A} = \frac{\partial \hat{E}}{\partial q}$).

The two-factor implicit algorithm involves two sweeps through the grid at each time step. The first sweep involves inverting the block tridiagonal system of equations shown in equation 15 along constant η grid lines to determine the intermediate solution variable $\hat{q}^*$. During the second sweep, a second block tridiagonal system of equations (equation 16) is inverted along grid lines of constant ζ to determine the dependent variable $\Delta \hat{q}^n$. The two-factor implicit algorithm reduces the computational requirements of the approach compared with the three-factor, central-difference, implicit algorithm of Beam and Warming (*11*). The algorithm contains additional numerical smoothing terms, $D_i|_\eta$, $D_i|_\zeta$, and D_e, to suppress numerical oscillations associated with the odd-even decoupling produced by the central differencing in the η and ζ directions (*7*).

2.2 Chimera Composite Overset Structured Grids

To more easily model the geometry and resolve the flow physics associated with the lateral jet problem, the Chimera composite overset grid technique has been applied. The Chimera technique is a domain decomposition approach that allows the entire flow field to be meshed into a collection of independent grids, where each piece is gridded separately and overset into a background grid. Overset grids are not required to join in any special way. Usually there is a major grid that covers the main domain (the external flow field about the projectile), and minor grids are generated to resolve the rest of the body or sections of the body. In current computations, a mixture of point-to-point zonal overlaps and Chimera overset gridding was utilized. As shown in figure 3, five large grid blocks with point-to-point zonal overlaps between blocks were used

to form the background grid around the munition body. Near the jet nozzle (figure 4) and on the fins (figures 5 and 6), Chimera overset grids were used to discretize the flow field near these geometric features.

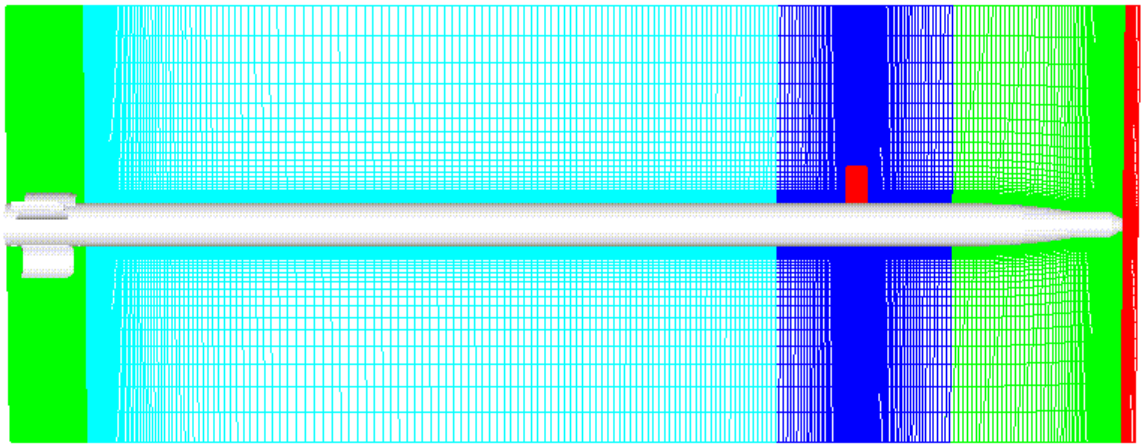

Figure 3. Overview of grid on 2.75-in testbed munition.

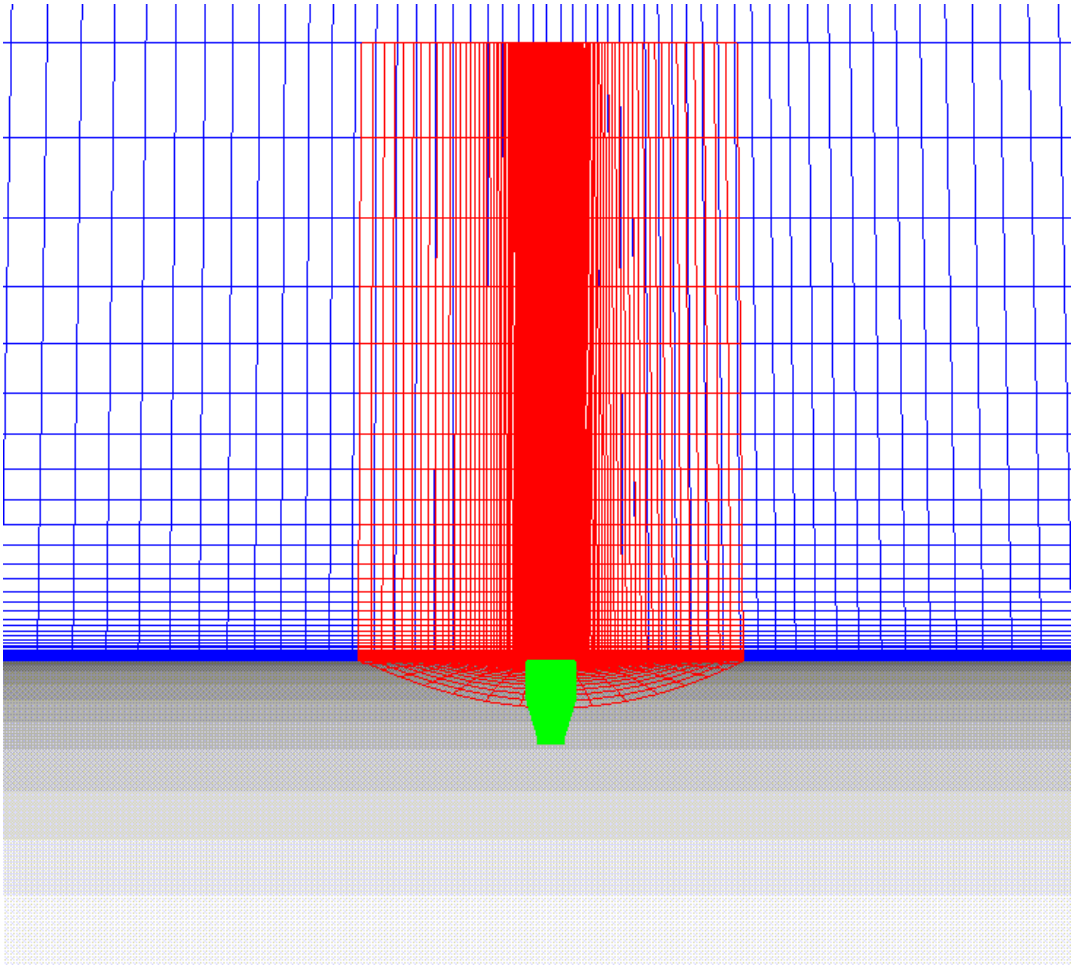

Figure 4. Overset grid system near jet nozzle.

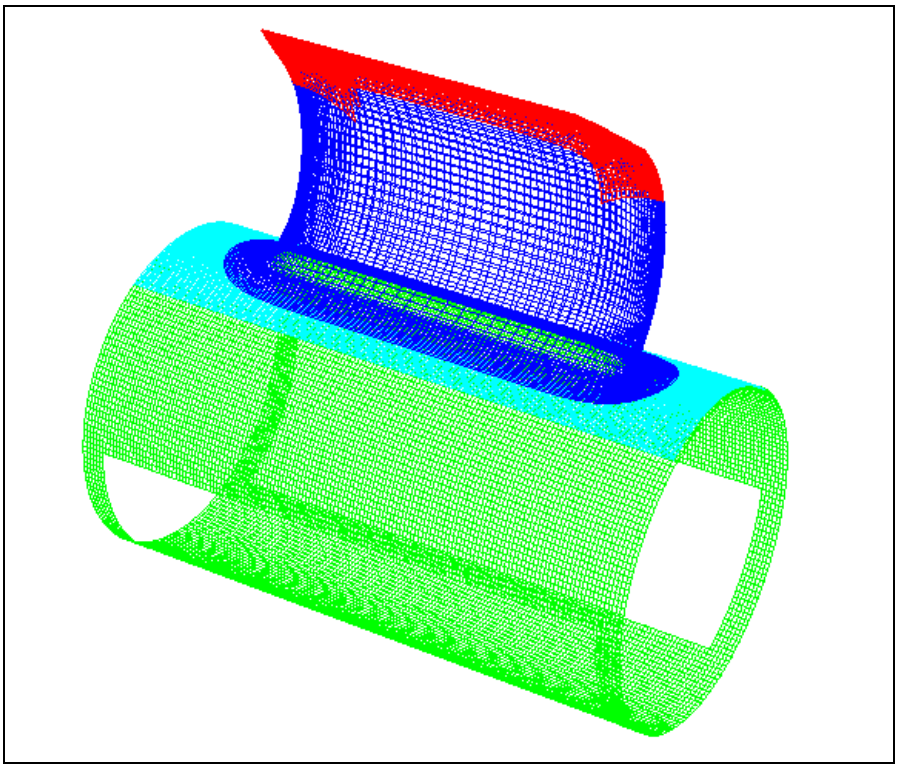

Figure 5. Overset grid system on surface of fin hub.

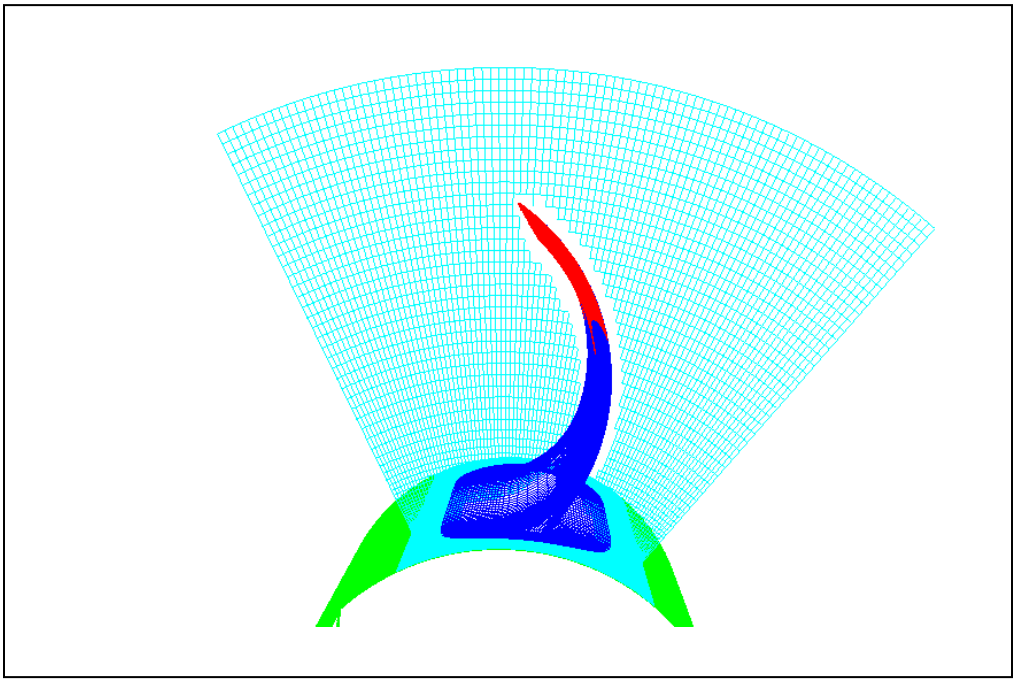

Figure 6. Overset grid system near fin hub.

Figure 4 displays the computational mesh near the nozzle region, showing the background grid for the projectile body along with an overset grid to better capture the physics of the jet interaction with the external flow. The overset jet grid is seen residing on top of the jet exit as a cylinder with a radius larger than the jet hole itself. A third grid, used to model the jet nozzle, resides underneath the jet grid. Point-to-point zonal overlaps are used for communication between the nozzle grid and the jet grid. A hole has been cut into the background grid by the scheme, and background grid points within the hole region are excluded from the solution process. The overset grid system used here for the jet region is very similar to that used in prior validation studies for the lateral control jet problem (*2*, *3*).

The computational model included the jet nozzle region downstream of the throat with the inflow plane located at the nozzle throat. Sonic flow was across at the throat of the nozzle, with a total temperature of 2500 K and a total pressure of 950 atmospheres. Subsequent calculations of the thrust produced at the nozzle exit (including contributions from the pressure at the nozzle throat, the momentum flux through the nozzle throat, and the pressure on the interior surface of the nozzle) indicated a jet-thrust impulse of 4.1 N-s over a duration of 6 ms. This correlated well with the nominal design impulse of 4 N-s. Because of the high jet total pressure relative to the external freestream pressure, the flow in the nozzle throat and the resulting jet thrust were essentially independent of the external flow conditions examined here.

Figures 5 and 6 show portions of the computational mesh used on the fins. Each fin was embedded in a box grid, with two additional nearbody grids used to discretize the flow field on the main fin surface and on the fin tip. For the complete grid system, 11.5-million grid points were used with 7.1-million points on the fins. In some cases, the mirror-plane symmetry of the flow field on the axisymmetric forebody was exploited to reduce the number of grid points by ~20% for the supersonic flow results described.

The thin-layer Navier-Stokes equations, shown previously in equations 15–17, have been modified for the Chimera scheme (*12*). The single and overset grid versions of the algorithm are identical except for the variable i_b, which accommodates the possibility of having arbitrary holes in the grid. The array i_b has the values of either 0 (for hole points) or 1 (for conventional field points—a mesh point within the computational domain updated by the flow solver or boundary conditions). Thus, points inside a hole are not updated (i.e., $\Delta\hat{q}^n = 0$), and the solution values on intergrid boundary points are supplied via interpolation from corresponding solutions in the overlap region of neighboring grid systems (*13*).

A complete simulation of a single steady-state lateral jet firing took ~750 CPU hours on an SGI Origin 3000. The solutions were run in parallel using eight processors, and a parallel speed-up to 5.4 was obtained.

3. Results

The computational approach has been applied to investigate the performance of the lateral control jet on the testbed munition shown in figure 1 at a flight speed of Mach 2. All predictions were made at 0° angle of attack for ambient sea-level flight conditions. During the course of the testbed munition design process, various axial locations for the jet thrusters were proposed, including in-line tandem jets. Table 1 presents the jet axial locations for the two configurations examined here. Configuration 1 is a tandem jet configuration, with the jets located in the same circumferential plane as shown in figure 1. Configuration 2 is a single jet configuration. Analyses have been performed to assess both the steady-state performance of the lateral jet and the time-dependent evolution of the pulsed jet. Steady-state jet-on simulations are discussed first and provide a basis for examining the time-dependent pulsed jet results presented later.

Table 1. Axial locations of jet nozzles.

Axial location of Jet Nozzle From Nose (Calibers)		
Configuration	**Forward Jet**	**Rear Jet**
1	5.817	6.461
2	6.066	NA

Note: NA = not applicable.

As a baseline for comparisons, computations were first performed for a single jet firing of the forward-most jet of configuration 1. Fluid dynamic modeling of the cavity flow associated with the inactive rear jet is incorporated in the simulation. Figure 7 shows the pressure contours on the body surface and in a vertical plane containing the jet. The most apparent effect of the jet on the pressure field is in the vicinity of the jet itself. A close-up of the jet region is shown in figure 8. The high-pressure region in front of the jet and the low-pressure region behind the jet are readily apparent. Jet effects further downstream of the jet are less apparent in the pressure field, but the small asymmetries produced by the jet on the flow field downstream of the jet produce important aerodynamic effects that are apparent in the force's distribution.

Figure 9 shows the jet interaction force distribution along the body. In the immediate vicinity of the jet (X/D = 5.8), there is a significant increase in the force distribution due to the high pressure near the jet nozzle produced by the flow field immediately behind the jet bow shock. Behind the jet, the force drops rapidly due to the combined effect of the low-pressure region behind the jet and the high-pressure region produced by the jet bow shock as it wraps around the body. Some recovery of the force is produced by the recompression downstream of the low-pressure region behind the jet. From the cylindrical portion of the body to the aft of the recompression, the jet interaction force shows relatively little variation. The interaction of the jet wake with the tail fins produces an additional reduction in the jet interaction force that is approximately the same

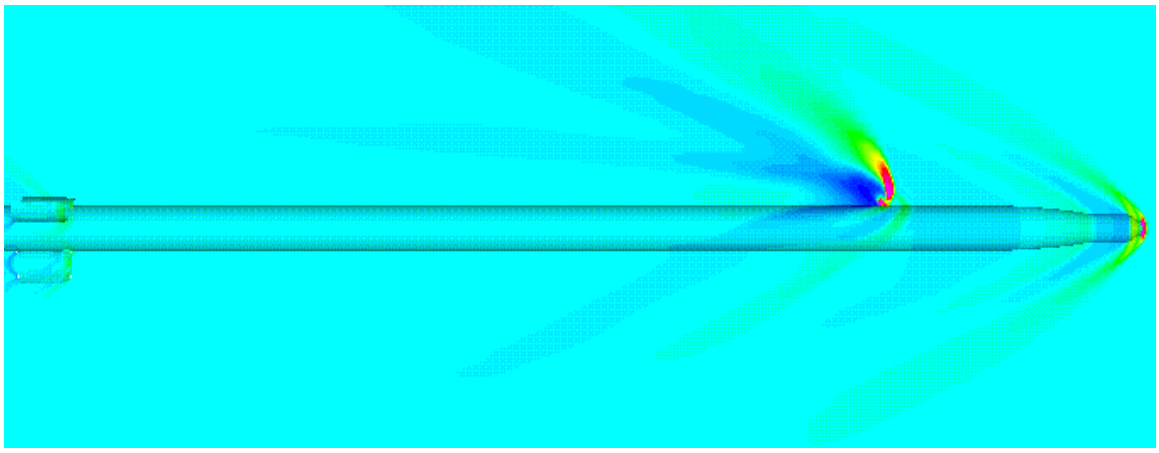

Figure 7. Pressure contours on 2.75-in rocket testbed, single jet.

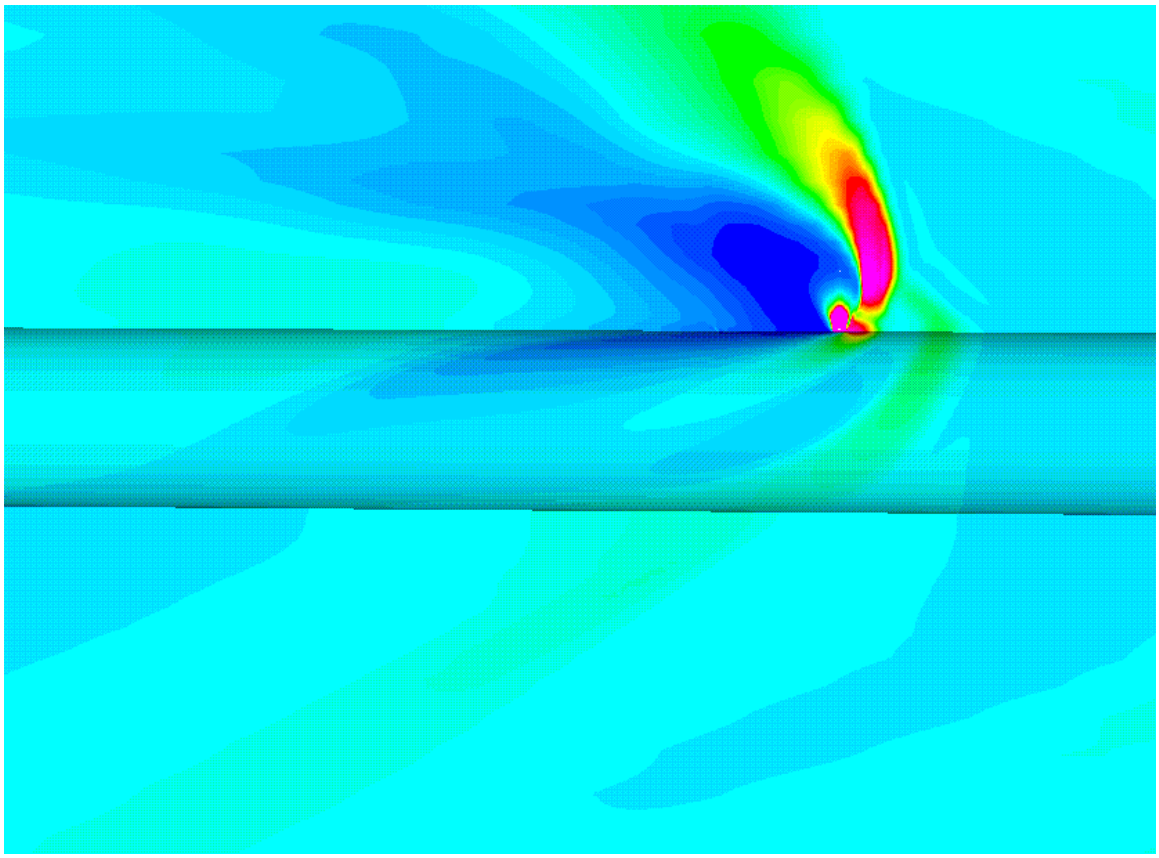

Figure 8. Pressure contours on 2.75-in rocket testbed, single jet, close-up of jet region.

magnitude as the jet interaction force on the cylindrical portion of the body. The net jet interaction force for the complete body is negative, indicating that the jet interaction opposes the thrust produced by the jet.

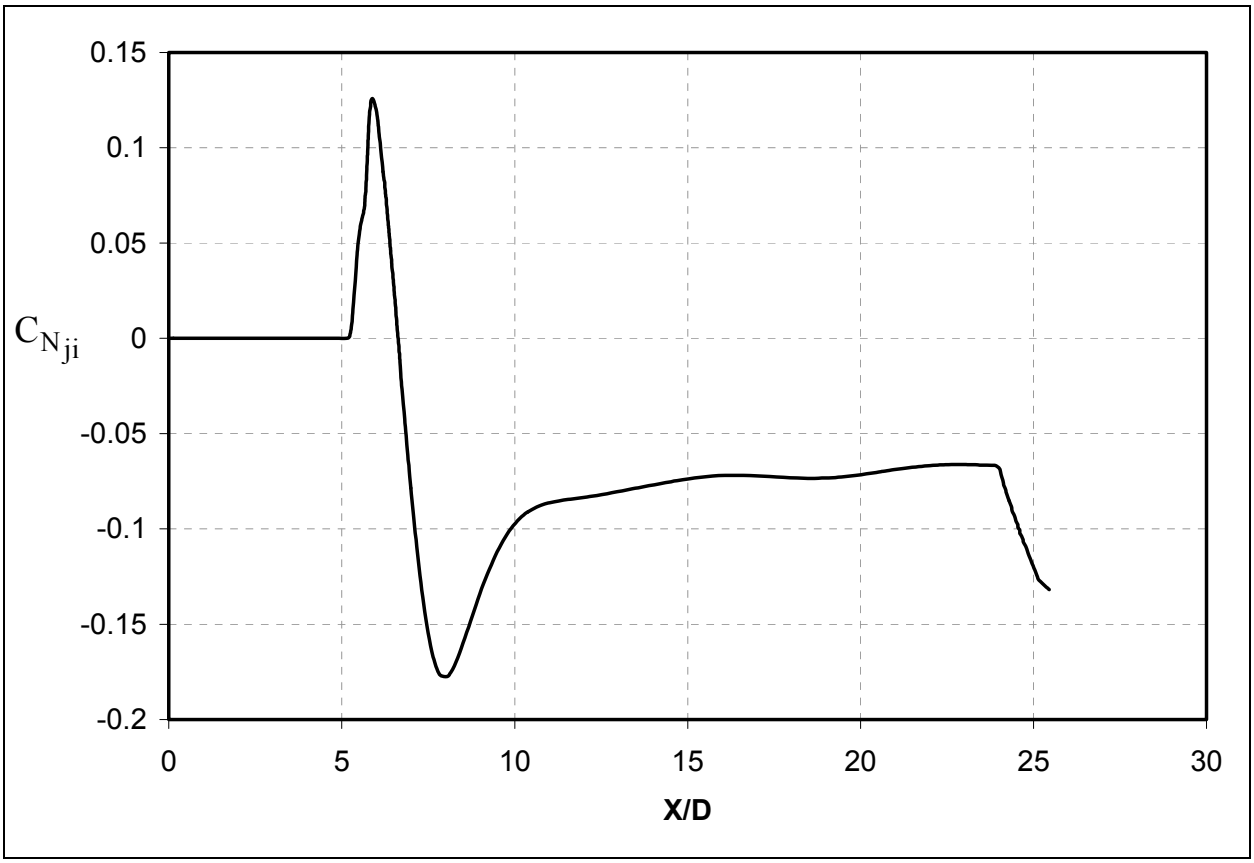

Figure 9. Jet interaction force distribution along length of body, single nozzle.

The jet interaction force generated by the tailfins appears, from flow-visualization studies, to be due to a small local angle of attack produced by the jet wake. This local angle of attack is oriented such that a lift force is produced on the fins that oppose the jet thrust. The local angle of attack varies as a result of a velocity gradient across the wake.

As discussed previously, the jet interaction amplification factor provides a means of assessing the size of the jet interaction force relative to the force produced by the jet thrust itself. For the single nozzle case, a jet amplification factor of K = 0.79 was computed, indicating that the effective thrust produced by the jet is reduced by 21% due to the jet interaction effect.

Although these lateral control jets produce control forces, the moment can be an important contributor for altering the trajectory due to the aerodynamic jump produced by the resulting angular rate (*14*). As previously shown, the jet interaction force has two important contributors—on the body near the jet and on the fin hub. Each of these reduce the effective jet force. However, when the moment is considered, both the direction of the applied force and the location of the applied force relative to the center of gravity are important. In this case, the contribution to the jet interaction moment on the body near the jet opposes the moment produced by the jet while the contribution to the jet interaction moment from the fin hub provides a moment component that augments to the moment produced by the jet thrust. The jet interaction

moment produced by the fin hub is more significant than that from the body because of the large moment arm between the center of gravity and the fin hub. The amplification factor for the moment of $K_m = 1.18$ was computed for this case, indicating that the moment is increased by 18% compared with the moment produced by the jet thrust itself.

The predicted results demonstrate that the interaction of the jet wake with the tailfins plays an important role in the overall effectiveness of the jet, despite the large distance between the fins and the jet nozzle. As discussed previously, the jet wake produces an asymmetrical velocity gradient across the flow field near the fin hub. It is therefore likely that the orientation of the fins relative to the jet may be an important variable in the overall performance of the jet.

In the current study, two tailfin orientations have been considered, as shown in figure 10. In orientation 1, the center of the jet wake passes between two adjacent fins. In orientation 2, the fins are rotated 60° with respect to orientation 1 so that one of the fins is close to the center of the jet wake. The results shown previously in figures 7–9 correspond to fin orientation 1.

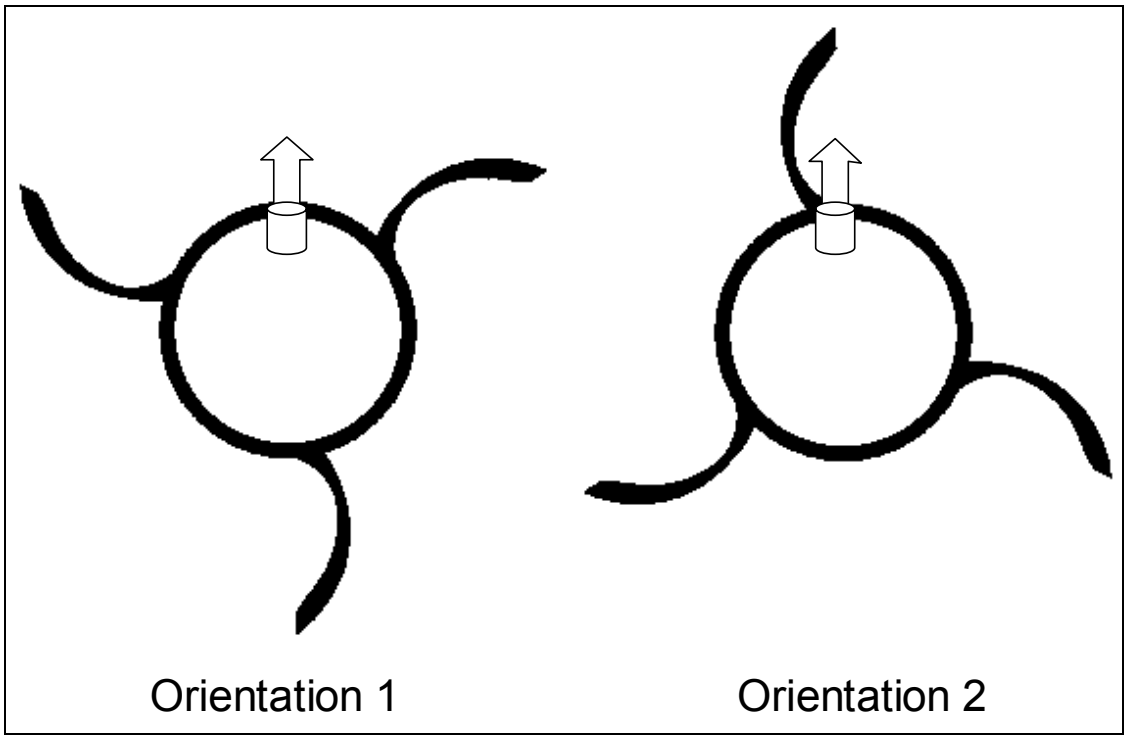

Figure 10. Schematic showing orientation of jet nozzle relative to the fins.

Figure 11 shows a comparison of the jet interaction force distribution along the body for both fin orientations. In front of the fins, the jet interaction force is unaffected by the fin orientation. However, on the fin hub, the jet interaction force is significantly different for the two fin orientations, with a significant reduction in the jet interaction force for the second fin orientation. Jet interaction force and moment amplification factors of $K = 0.87$ and $K_m = 0.91$ were computed for fin orientation 2. While the differences in the net jet forces between the two fin orientations

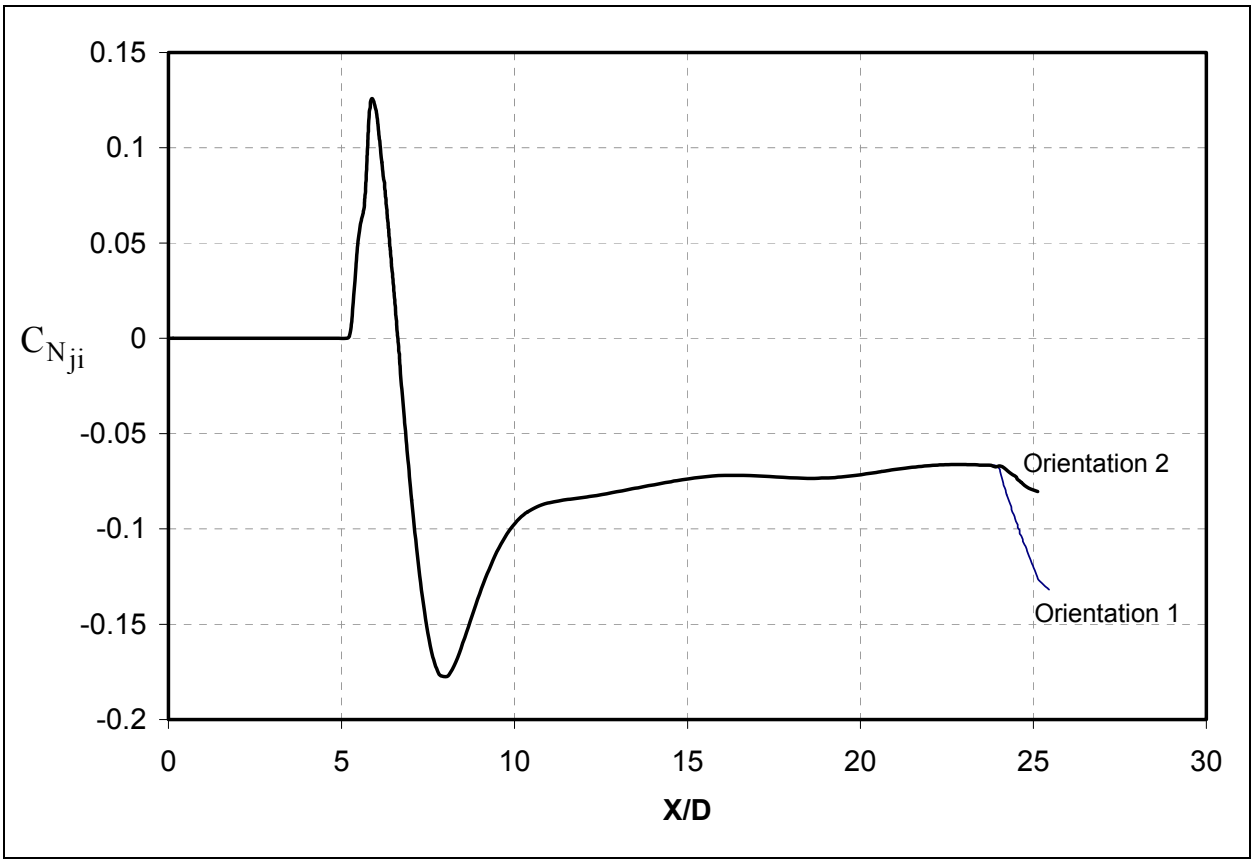

Figure 11. Comparison of jet interaction force distribution along length of body, single nozzle, fin orientations 1 and 2.

is 10%, there is nearly a 30% difference in the net moment with amplification of the moment for orientation 1 and deamplification for orientation 2.

For some of the firings, it was envisioned that two lateral control jets would be firing in tandem to increase the net control force. The predictive technique was applied to determine the effectiveness of this configuration. Figures 12 and 13 show the predicted pressure contours produced by the simultaneous firing of the two lateral control jets. The fins are oriented in orientation 1 for these computations. Although the presence of the second jet is apparent in the plots of the pressure contours, the forward-located jet appears to produce the strongest effect in interacting and redirecting the oncoming flow.

Figure 14 shows a comparison of the distribution of the jet interaction force along the body for both the single and dual jet configurations. The rearward-located jet appears to have little influence on the force distribution in the vicinity of the forward-most jet. However, the effect of the second jet is much stronger in the low-pressure region behind the jets producing a larger jet interaction force that opposes the jet thrust. The effect of the wake on the tail fins is also stronger for the dual jet configuration producing an additional force deamplification. The net effect of dual jet firings is to produce approximately twice the net force of the single jet. Jet

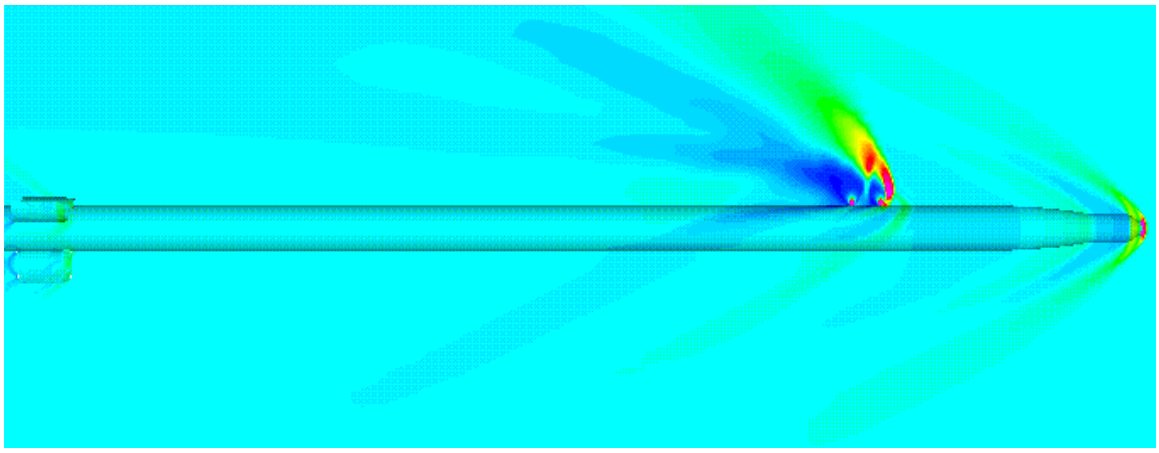

Figure 12. Pressure contours on 2.75-in rocket testbed, dual jet.

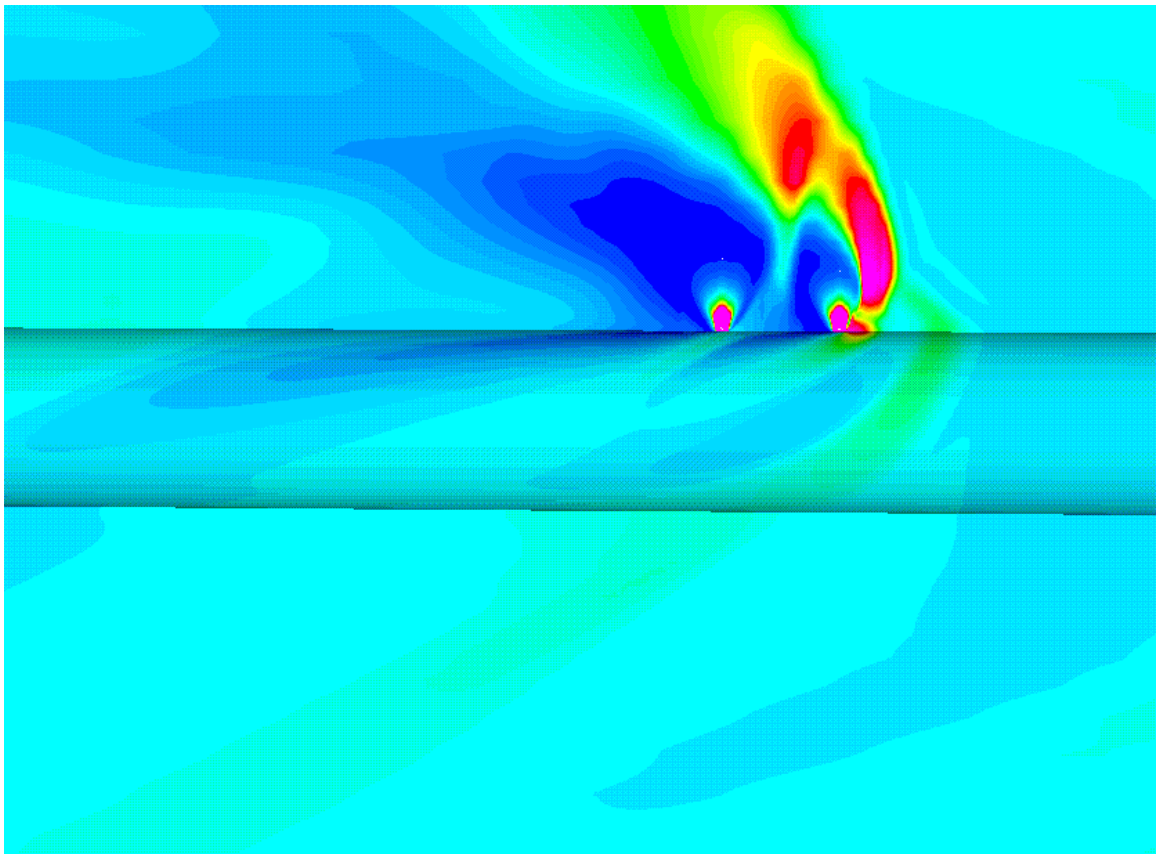

Figure 13. Pressure contours on 2.75-in rocket testbed, dual jet, close-up of jet region.

interaction force and moment amplification factors of K = 0.82 and K_m = 1.17 were computed for this configuration, which are very similar to the results obtained for the single nozzle results for fin orientation 1. Although the dual jet firings produce approximately twice the net force and moment of a single jet, these results indicate that there is no significant benefit or disadvantage

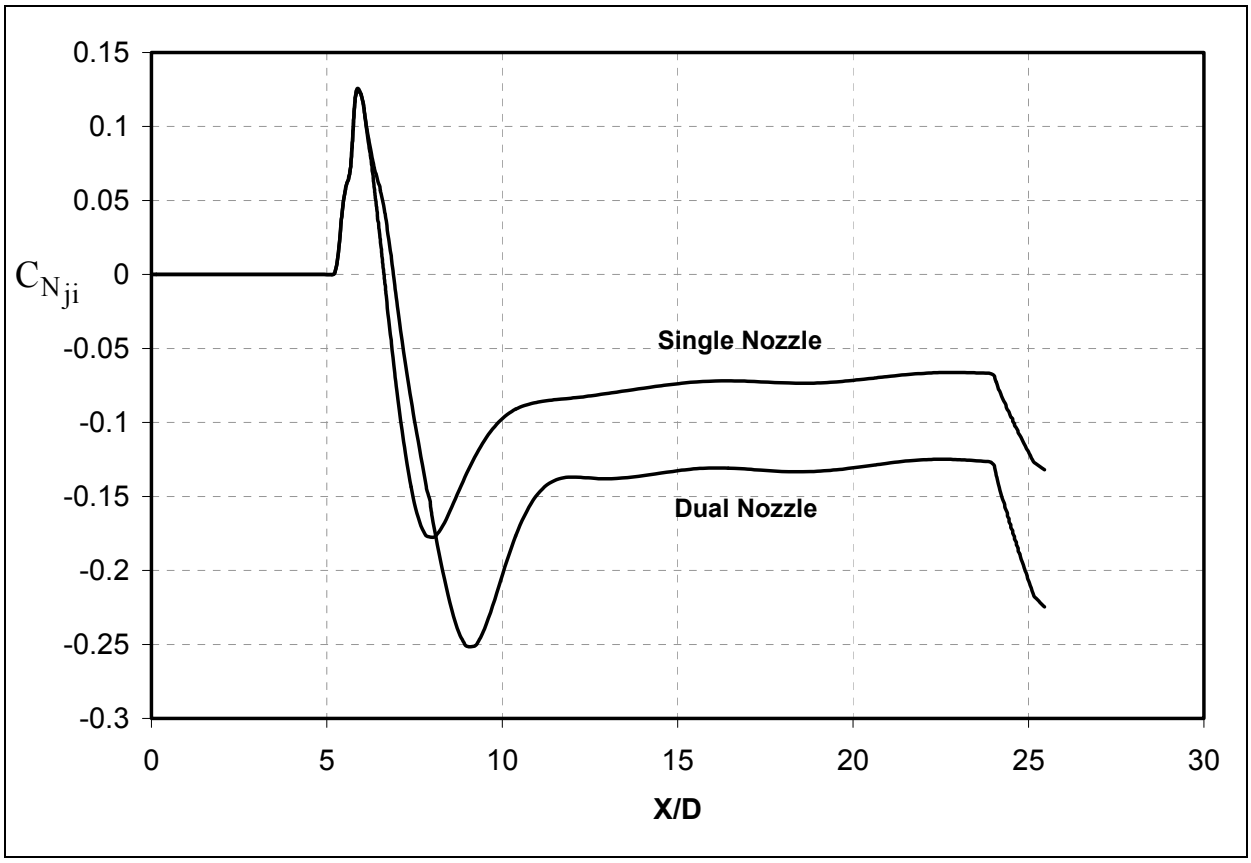

Figure 14. Comparison of jet interaction force distribution along length of body, single and dual nozzles.

of simultaneous firings of the dual lateral control jet compared with sequential firings of the same jets as far as the resulting control force and moment.

Typically, the 2.75-in rocket testbed flies with a small roll rate due to the geometric and aerodynamic asymmetries of the fins. Trajectory simulations indicate that the expected roll rate is ~ –20 rev/s (counterclockwise rotation of 20 rev/s when viewing the flight body looking downrange) for the testbed munition at Mach 2. Predictions of the effect of roll rate on the lateral control jet performance were made using the computational procedure. Figure 15 shows a comparison of the distribution of the jet interaction normal force along the body for 0, –20, and –215 rev/s. Compared to the zero-roll rate results, there is almost no effect of roll rate on the lateral jet performance at –20 rev/s. This is not too surprising because the fins rotate only about 15° in the time it takes for a fluid particle to travel the distance from the jet to the fin hub. However, roll rate effects can become more significant if the roll rate is increased. Figure 15 also shows the jet interaction normal force distribution for a roll rate of –215 rev/s, which is an order of magnitude higher than the expected roll rate. Most of the difference occurs several calibers downstream of the jet and on the fins. In particular, the jet interaction force near the recompression region behind the jet shows a somewhat-larger deamplification compared with the lower spin rates. In part, this is due to the fact that the recompression region has rotated around

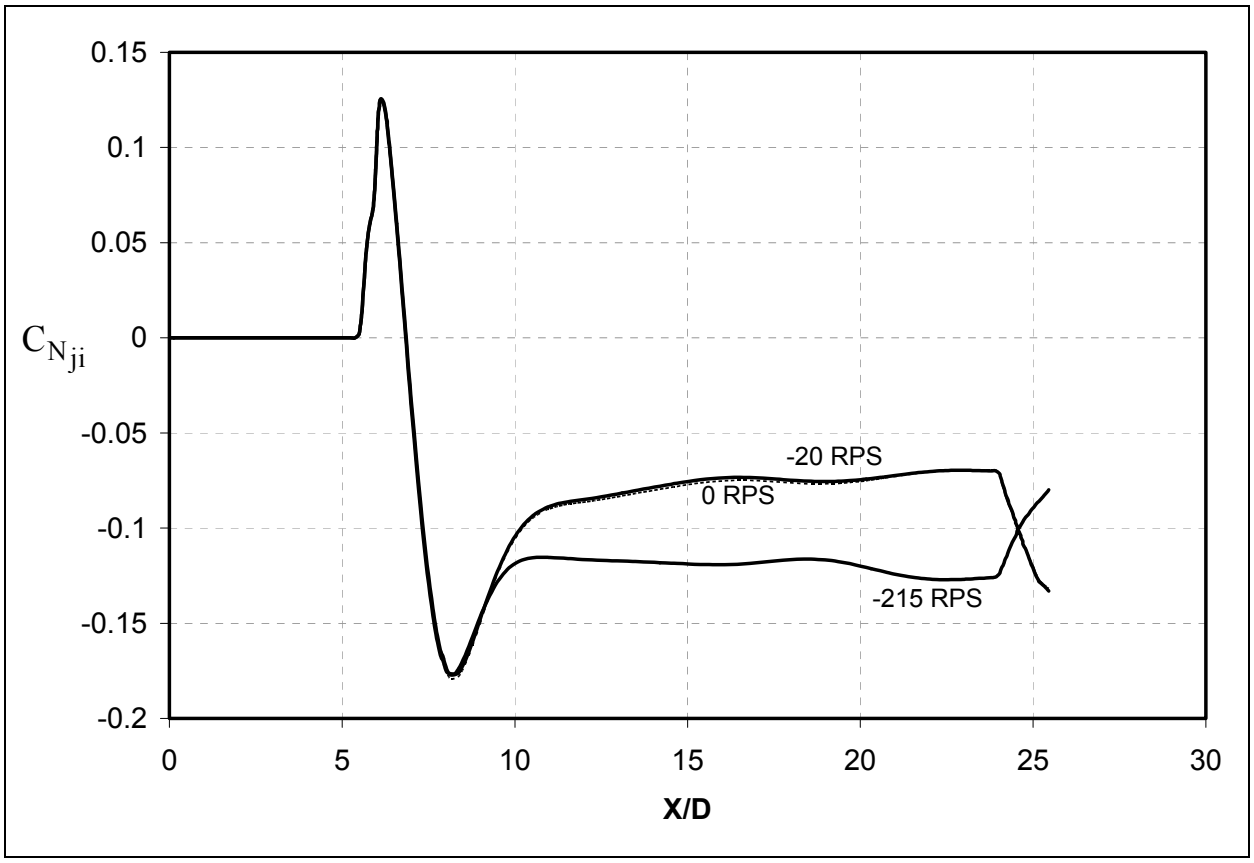

Figure 15. Effect of roll rate on jet interaction force distribution along length of body, configuration 2.

the body and acts on the side of the body rather than on the top. This rotation of the flow field as it interacts on the fins also produces an amplification of the jet interaction normal force on the fins instead of the deamplification observed for the 0 and –20 rev/s spin rates.

The rotation of the jet interaction flow field due to the spin can be seen in the surface pressure profiles shown in figure 16. At the –20 rev/s spin rate, the flow field is nearly symmetric. As the spin rate increases to –215 rev/s, the asymmetries behind the jet produced by the spin rate become more apparent.

The asymmetries in the surface pressure on the axisymmetric part of the body produce a side force as shown in figure 17. Due to symmetry, the side force on axisymmetric part of the body at zero spin rate is nonexistent, although a small side force is produced on the fins due to the asymmetric arrangement of the wraparound fins. A small side force is produced as the spin rate is increased to –20 rev/s. However, this side force is quite small compared with the zero-spin jet interaction normal force also displayed on this figure. For the larger spin rate of –215 rev/s, the side force produced by the jet interaction becomes much larger and has nearly the same magnitude as the jet interaction normal force for this spin rate. The additional side force produced by the jet interaction results in a misalignment of the total force produced by the jet.

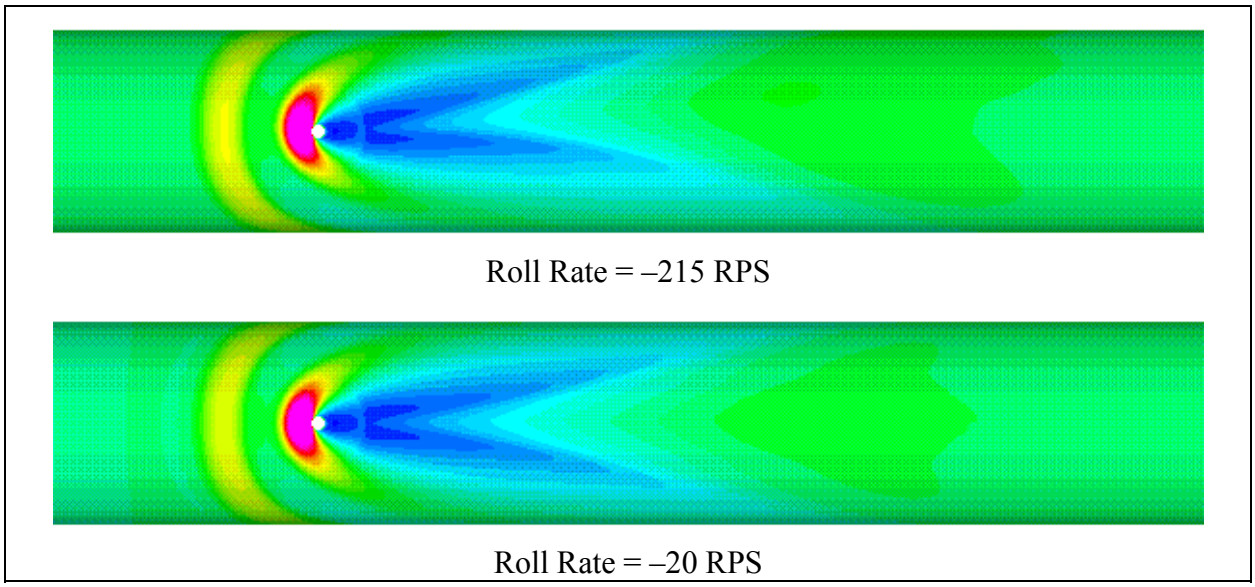

Figure 16. Pressure contours near jet, –20 and –215 rps roll rates, configuration 2.

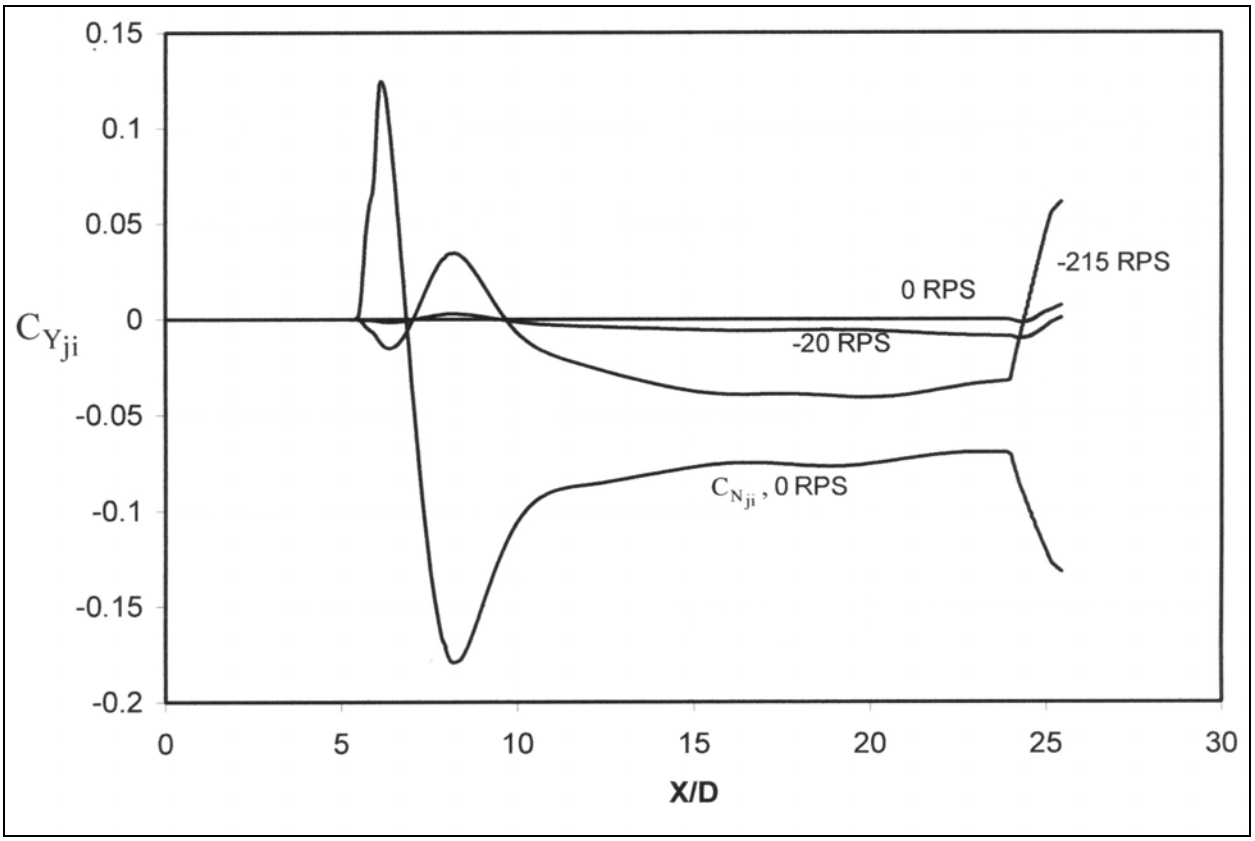

Figure 17. Comparison of jet interaction normal and side force distributions along length of body, –20 and –215 rps roll rates, configuration 2.

Based on the computed jet interaction side and normal forces and the jet thrust, this misalignment is ~5° for the –215 rev/s spin rate.

As noted previously, for the current application, the lateral control jet is pulsed over a short duration (6 ms). To properly assess the performance of the pulsed jet, time-dependent computations were executed to quantify the time-dependent response of the jet using configuration 2. Steady-state jet-on computations were also performed for configuration 2 as a baseline for comparison, although only slight differences where found between configuration 2 and the single-jet configuration 1 results presented previously. Figures 18 and 19 show the pressure contours during the jet-on and jet-off transients. During the jet-on transients, the disturbance produced by the jet effects the flow field nearest the jet first and gradually sweeps down the body to the tailfins. During the jet-off transients, again the flow field nearest the jet is effected first and the disturbances are gradually convected downstream to the tailfins as the flow field returns to the jet-off steady state.

Figure 20 shows the jet thrust, the jet interaction force, and total force coefficients as a function of time. The results show that after ~2.5 ms, a steady-state jet-on flow field was obtained. This was ascertained by monitoring the jet interaction force distribution along the body until steady-state was reached. The results were also compared with the steady-state results discussed previously. It should be noted that 2.5 ms is approximately the same time required for a fluid particle in the undisturbed freestream to travel the length of the body. After 6 ms, the jet is turned off and an additional 2.5 ms are required for the flow field to return to the steady-state jet-off flow. For ~1.5 ms after the jet is turned on or turned off, the variation in the jet interaction force is predominately on the axisymmetric part of the body and the forces on the fins are relatively unaffected because the disturbances from the jet have not reached the fins. The transients 1.5 ms after the jet is turned on or off are for the most part due to transients on the fins, although some transients on the body are still apparent as steady flow is established on the entire body.

Jet interaction linear and angular impulse amplification factors of $I = 0.72$ and $I_m = 1.21$ were computed for the time-dependent pulsed jets. These compare favorably with the jet interaction force and moment amplification factors for the steady-state jet for the same configuration. Essentially, the linear and angular impulses produced by the time-dependent pulsed jet are similar to the impulse that would be produced if the steady-state jet force and moment were to be applied over the 6-ms duration of the pulsed jet. Because the jet interaction force takes some time to develop when the jet is turned on and off, the linear impulse due to the pulsed jet occurs slightly earlier than if the jet force acted as a square-wave pulse over the 6-ms duration of the jet pulse.

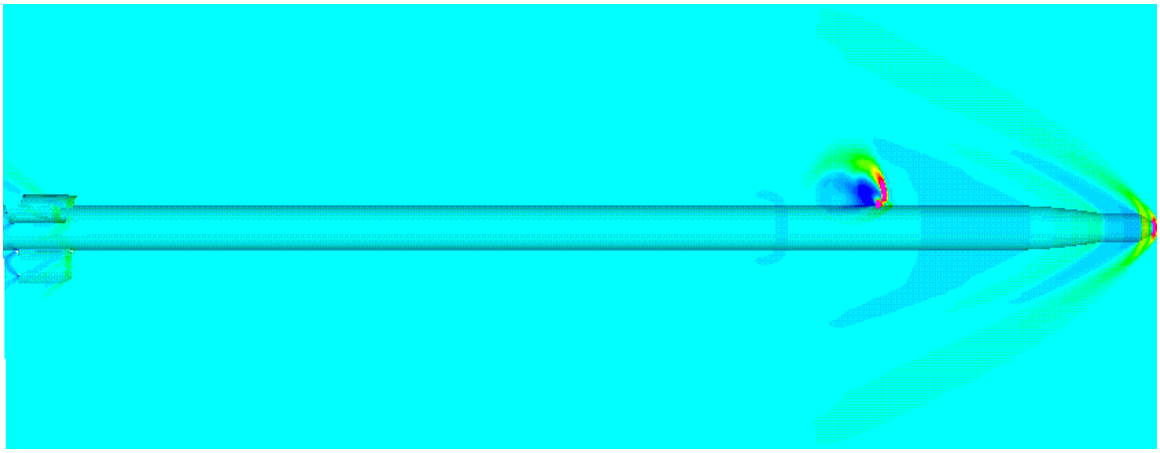

(a) 0.1 ms

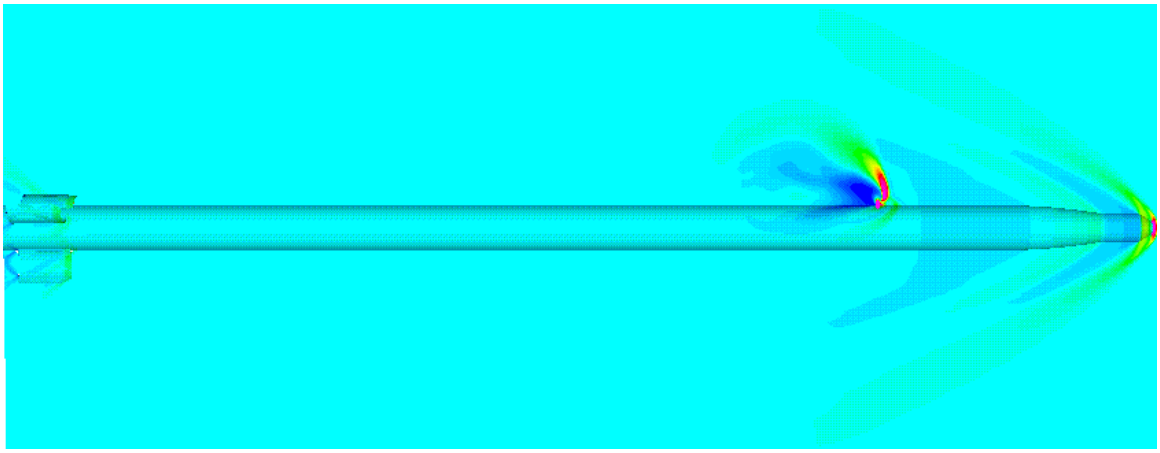

(b) 0.25 ms

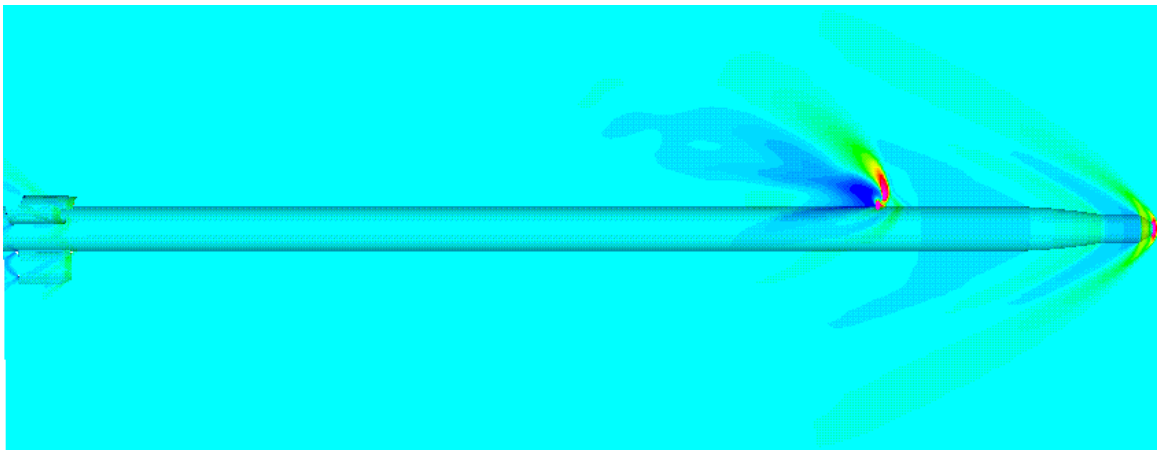

(c) 0.5 ms

Figure 18. Time-dependent pressure contours during jet-on transient.

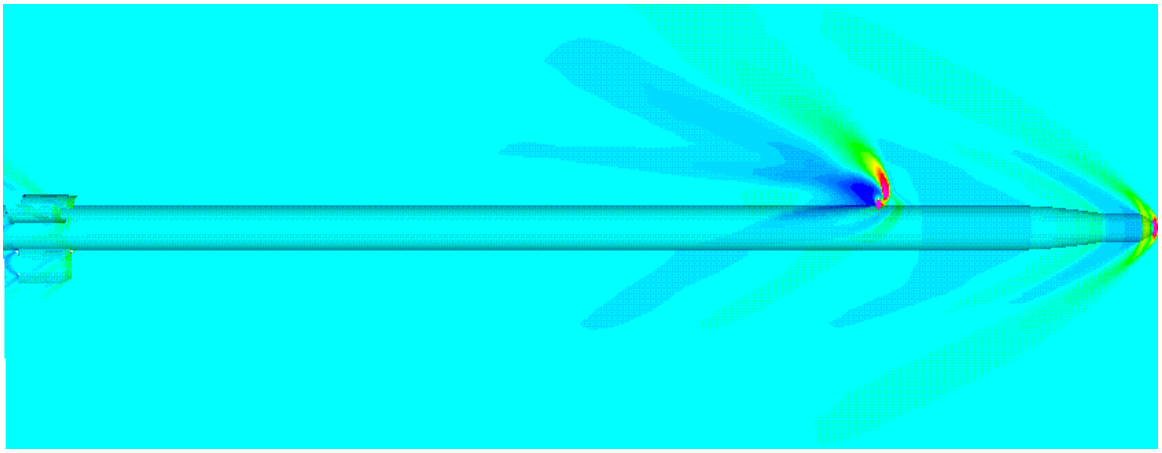

(d) 1.0 ms

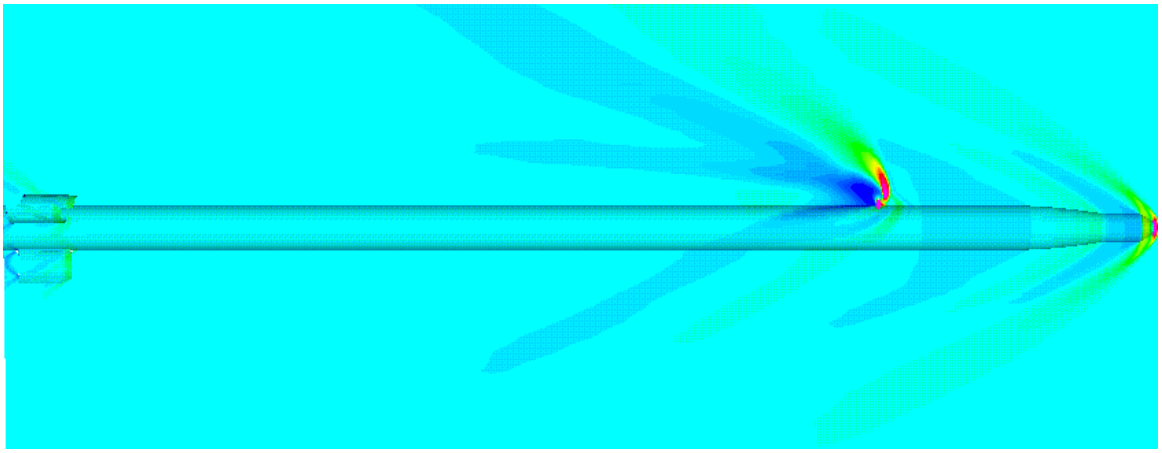

(e) 1.5 ms

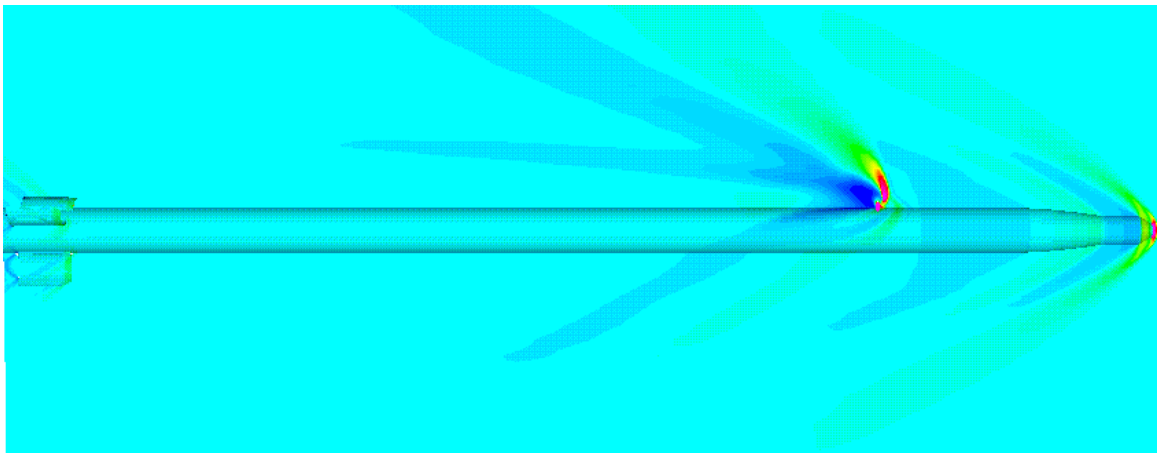

(f) 2.5 ms

Figure 18. Time-dependent pressure contours during jet-on transient (continued).

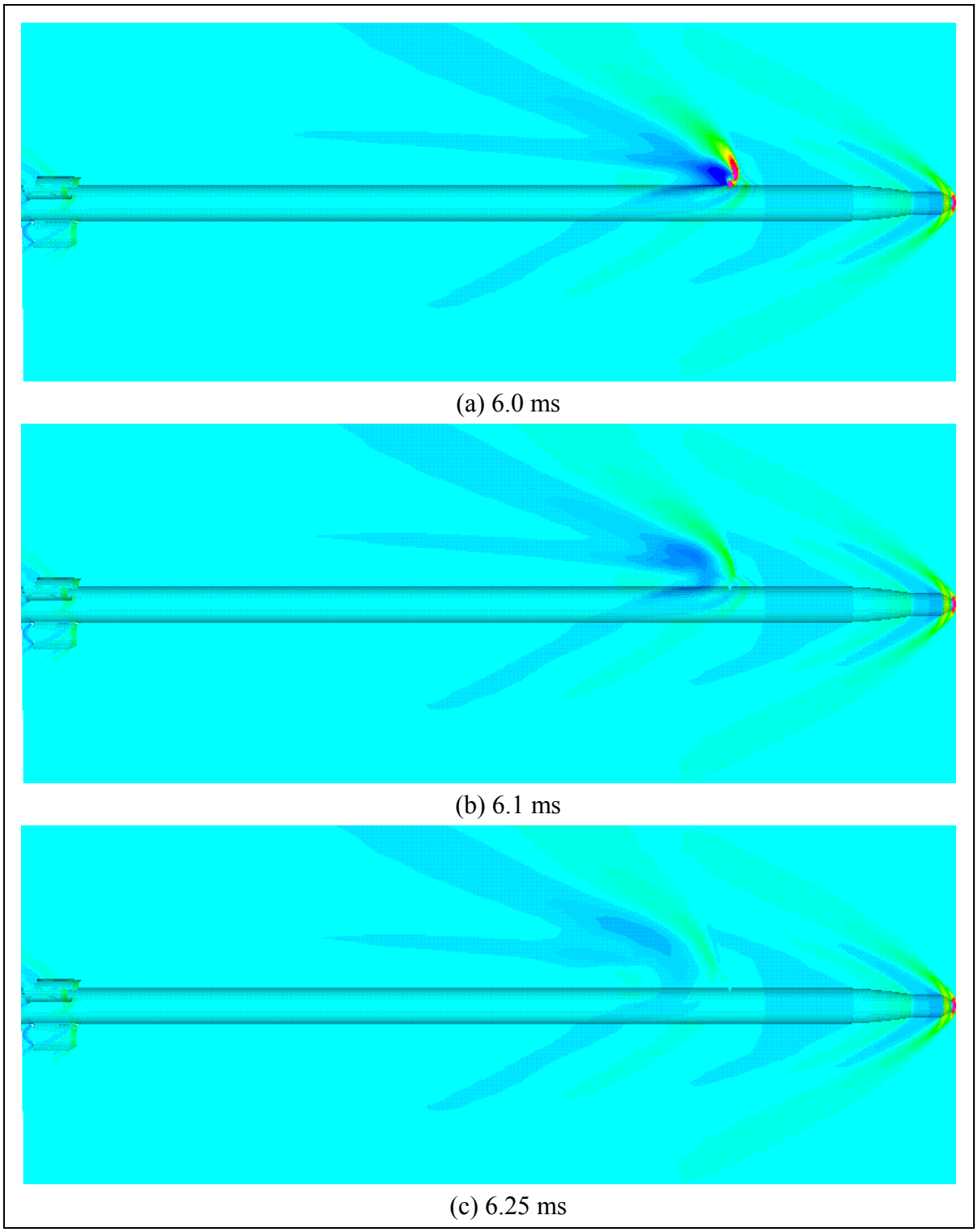

(a) 6.0 ms

(b) 6.1 ms

(c) 6.25 ms

Figure 19. Time-dependent pressure contours during jet-off transient.

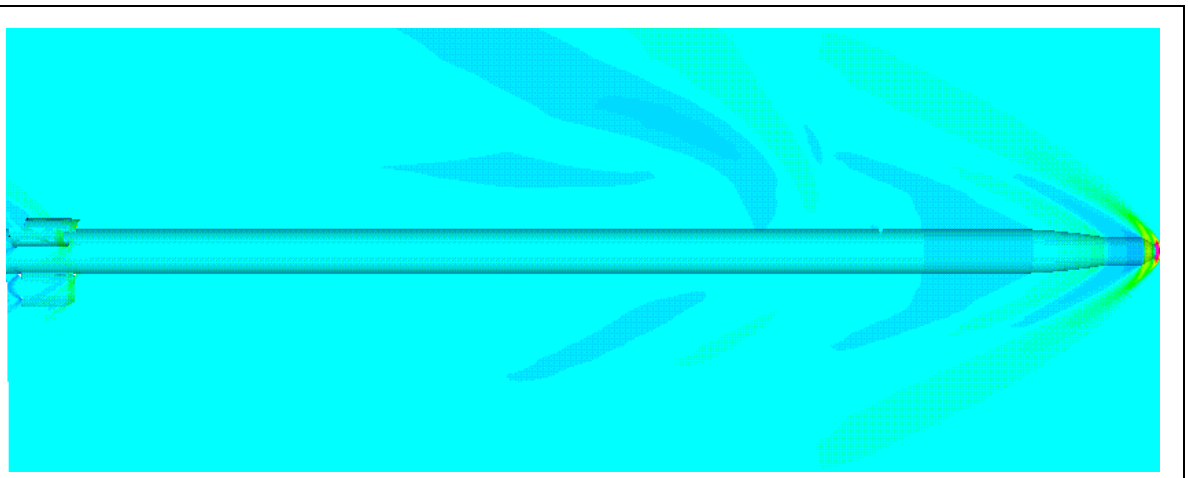

(d) 6.5 ms

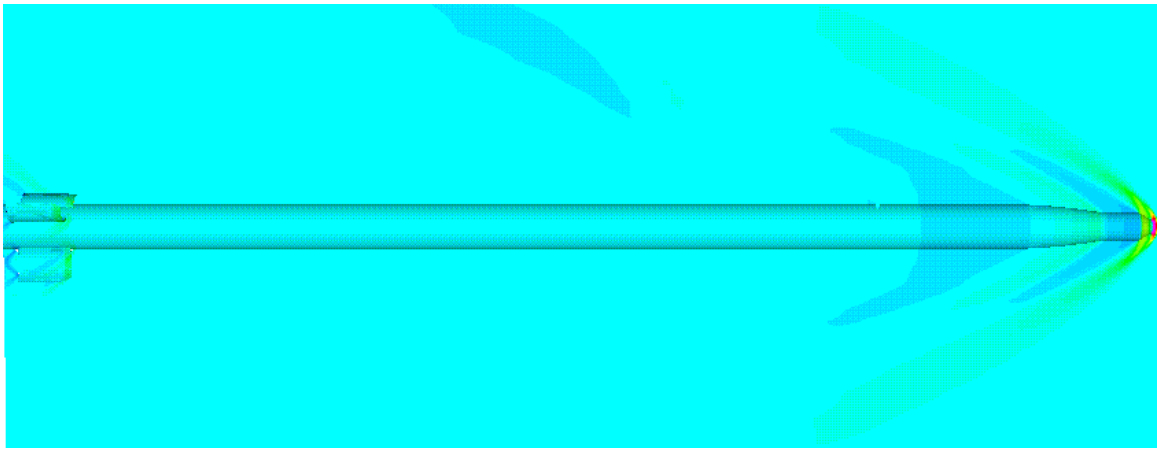

(e) 7.0 ms

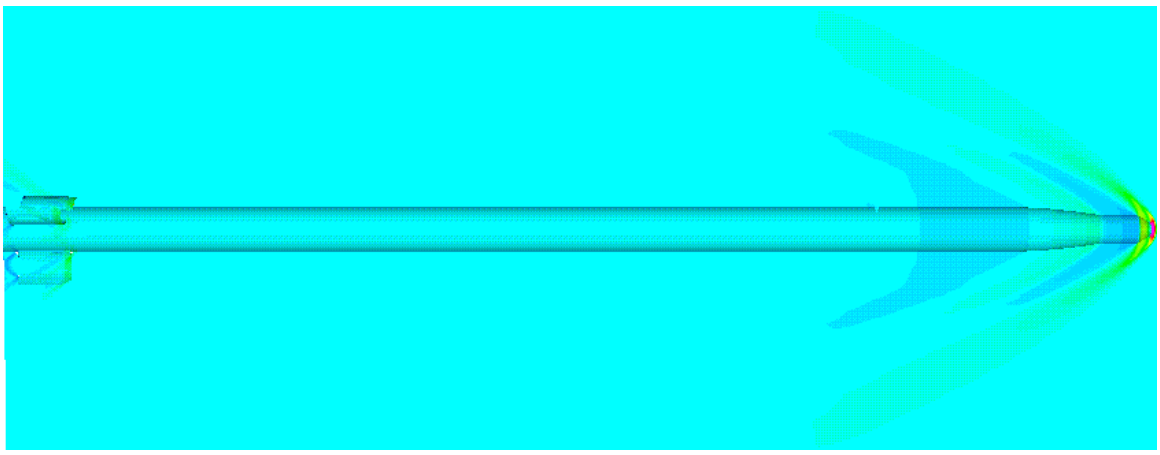

(f) 10.0 ms

Figure 19. Time-dependent pressure contours during jet-off transient (continued).

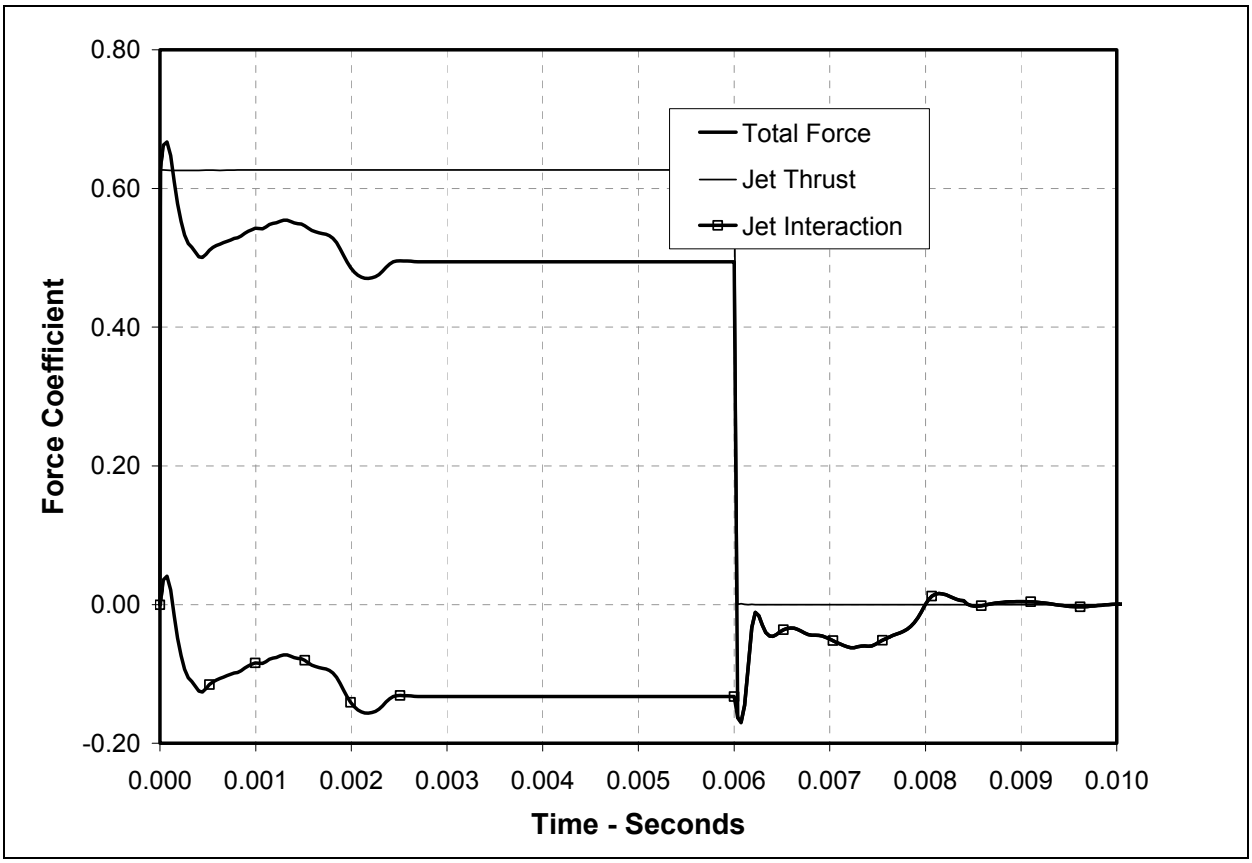

Figure 20. Variation of jet thrust, jet interaction force, and total force as a function of time, single nozzle.

4. Summary

The aerodynamic performance of lateral control jets for a testbed munition has been investigated using a sophisticated numerical technique. Using the numerical approach, the interaction of the jet with the external flow around the munition has been captured and its effect on the lateral control jet performance has been assessed. Important design variables such as single and tandem jet geometries, tail fin orientation relative to the jet, and munition spin rate have been investigated. Both steady-state and time-dependent pulsed jet performances have been predicted using the computational approach.

The forces and moments produced by the interaction of the jet with the external flow over the body were significant contributors to the total force and moment produced by the lateral control jets. Thus, benchtop characterization of the jet thrust yielded only a portion of the total force produced by the jet. The most significant jet interaction forces and moments were created on two distinct parts of the body. Near the jet, the high pressure around the jet orifice and the low pressure in the wake jet behind the jet interacted to produce competing forces that for the flow

conditions presented here produced a net deamplification or reduction of the thrust produced by the jet. Significant forces and moments were also produced by the interaction of the jet wake with the tail fins of the testbed munition. The relative magnitude of the forces and moments on the tail fins was found to be dependent on factors such on the geometric orientation of the fins relative to the jet and projectile spin rate. In some cases, amplification of the jet moment was observed even when force deamplification occurred, due to the interaction of the wake with the rear mounted tail fins.

The fin orientation relative to the jet was also found to be an important parameter in the performance of the lateral control jets. When one of the fins was aligned in the same circumferential plane as the jet, deamplification of jet force and moment was observed. However, when the fins were oriented such that the circumferential plane containing the jet was located between adjacent fins, a net amplification of the jet moment was observed, increasing nearly 30% compared with the other fin orientation.

The effect of spin on the performance of the lateral control jets was also investigated. For the expected range of spin rates for the testbed munition, the predictions showed that spin rate had very little effect on the performance of the lateral control jets. However, if the spin rate was increased to an order of magnitude, the performance of the lateral control jet showed a much larger dependence on the spin rate including a misalignment of the net thrust relative to the jet nozzle.

A tandem jet arrangement was also investigated as a means of increasing the control authority by firing multiple jets simultaneously. The results showed a doubling of net force produced by tandem jet firings. While doubling of the jet thrust was expected, the results showed that the jet interaction force also doubled, resulting in nearly identical jet force amplification factors for the tandem jet arrangement compared with the single jet configuration. The implication here was that no synergistic effect was observed for the tandem jet firings, and virtually the same net jet force could be obtained by sequential firings of the individual jets.

Time-dependent computations were also performed to assess the performance of the pulsed jets. The predictions showed that steady-state flow fields were obtained for about half of the 6 ms duration of the jet pulse. During the transient phases of start up and shut down of the jets, the transient effects were observed first near the nozzle and lastly on the tail fins on the aft of the body. The jet interaction linear and angular impulse factors for the pulsed jets were very similar to the jet interaction amplification factors for the steady-state jets. Thus, the steady-state jet results could be used to provide meaningful assessments of the performance of the pulsed jets.

5. References

1. Brown, T. G.; Muller, P.; Brosseau, T.; Weinacht, P.; Childers, M.; Newill, J. Accuracy Control of a Rocket. *Proceedings of the 20th International Symposium on Ballistics*, Orlando, FL, 23–27 September 2002.

2. Graham, M. J.; Weinacht, P. Numerical Investigation of Supersonic Jet Interaction for Axisymmetric Bodies. *Journal of Spacecraft and Rockets* **2000**, *37* (5), 675–683.

3. Graham, M. J.; Weinacht, P.; Brandeis, J. Numerical Investigation of Supersonic Jet Interaction for Finned Bodies. *Journal of Spacecraft and Rockets* **2002**, *39* (3), 376–383.

4. Pulliam, T. H.; Steger, J. L. On Implicit Finite-Difference Simulations of Three-Dimensional Flow. *AIAA Journal* **1982**, *18* (2), 159–167.

5. Baldwin, B. S.; Lomax, H. *Thin Layer Approximation and Algebraic Model for Separated Turbulent Flows*. AIAA Paper 78-257; 16th AIAA Aerospace Sciences Meeting, Huntsville, AL, January 1978.

6. Cebeci, T. *Calculation of Compressible Turbulent Boundary Layers With Heat and Mass Transfer*. AIAA Paper 70-741; June–July 1970.

7. Ying, S. X.; Steger, J. L.; Schiff, L. B.; Baganoff, D. *Numerical Simulation of Unsteady, Viscous, High-Angle-of-Attack Flows Using a Partially Flux-Split Algorithm*. AIAA Paper 86-2179; AIAA 13th Atmospheric Flight Mechanics Conference, Williamsburg, VA, August 1986.

8. Sahu, J.; Steger, J. L. Numerical Simulation of Three-Dimensional Transonic Flows. *International Journal for Numerical Methods in Fluids* **1990**, *10*, 55–873.

9. Steger, J. L.; Warming, R. F. Flux Vector Splitting of the Inviscid Gasdynamic Equations With Application to Finite-Difference Methods. *Journal of Computational Physics* **1981**, *40*, 263–293.

10. Steger, J. L.; Buning, P. *Developments in the Simulation of Compressible Inviscid and Viscous Flow on Supercomputers*. NASA TM 86674, Moffett Field, CA, 1985.

11. Beam, R.; Warming, R. F. An Implicit Factored Scheme for the Compressible Navier-Stokes Equations. *AIAA Journal* **1978**, *16* (4), 85–129.

12. Benek, J. A.; Donegan, T. L.; Suhs, N. E. *Extended Chimera Grid Embedding Scheme With Application to Viscous Flows*. AIAA Paper No. 87-1126-CP, 1987.

13. Meakin, R. L. Composite Overset Structured Grids. In *CRC Handbook of Grid Generation*; CRC Press, Inc.: Boca Raton, FL, 1997.

14. Guidos, B. J.; Cooper, G. R. *The Effect of a Simple Lateral Impulse on Kinetic Energy Projectiles in Flight*. ARL-TR-2076; U.S. Army Research Laboratory: Aberdeen Proving Ground, MD, December 1999.

List of Abbreviations and Symbols

C_N	Normal force coefficient, $\frac{F}{\frac{1}{2}\rho V^2 S_{ref}}$
$C_{N_{ji}}$	Jet interaction normal force coefficient
$C_{Y_{ji}}$	Jet interaction side force coefficient
D	Reference diameter
e	Total energy per unit volume
$\hat{E}, \hat{F}, \hat{G}$	Flux vectors in transformed coordinates
$\vec{f}$	Acceleration vector due to rotating frame
f_x, f_y, f_z	Component of acceleration vector $\vec{f}$ in the x, y, and z directions
F	Force
F_j	Jet thrust
F_{ji}	Jet interaction force
F_{no-jet}	Jet-off force
$\hat{H}$	Source term in Navier-Stokes equations due to rotating coordinate frame
i_x	Unit vector along body longitudinal axis
I	Jet interaction linear impulse amplification factor
I_m	Jet interaction angular impulse amplification factor
J	Jacobian
K	Jet interaction force amplification factor
K_m	Jet interaction moment amplification factor
M_j	Moment due to jet thrust
M_{ji}	Jet interaction moment

p	Pressure, as used in Navier-Stokes equations
$\hat{q}$	Vector of dependent variables scaled by Jacobian
$\vec{R}$	Displacement vector between the axis of rotation and location in flow field
Re	Reynolds number, $a_\infty \rho_\infty D / \mu_\infty$
$\hat{S}$	Viscous flux vector
S_{ref}	Reference area, $S_{ref} = \frac{\pi D^2}{4}$
t	Time
u, v, w	Velocity components in the three coordinate directions
U, V, W	Contravariant velocity components
V	Reference velocity
x, y, z	Axial, horizontal, and vertical coordinates
X	Dimensional axial coordinate

Greek Symbols

γ	Ratio of specific heats
μ	Viscosity
ρ	Density
Ω	Roll rate of body/coordinate system
ξ, η, ζ	Transformed coordinates in Navier-Stokes equations

NO. OF COPIES	ORGANIZATION
1 (PDF Only)	DEFENSE TECHNICAL INFORMATION CENTER DTIC OCA 8725 JOHN J KINGMAN RD STE 0944 FT BELVOIR VA 22060-6218
1	COMMANDING GENERAL US ARMY MATERIEL CMD AMCRDA TF 5001 EISENHOWER AVE ALEXANDRIA VA 22333-0001
1	INST FOR ADVNCD TCHNLGY THE UNIV OF TEXAS AT AUSTIN 3925 W BRAKER LN STE 400 AUSTIN TX 78759-5316
1	US MILITARY ACADEMY MATH SCI CTR EXCELLENCE MADN MATH THAYER HALL WEST POINT NY 10996-1786
1	DIRECTOR US ARMY RESEARCH LAB AMSRD ARL D DR D SMITH 2800 POWDER MILL RD ADELPHI MD 20783-1197
1	DIRECTOR US ARMY RESEARCH LAB AMSRD ARL CS IS R 2800 POWDER MILL RD ADELPHI MD 20783-1197
3	DIRECTOR US ARMY RESEARCH LAB AMSRD ARL CI OK TL 2800 POWDER MILL RD ADELPHI MD 20783-1197
3	DIRECTOR US ARMY RESEARCH LAB AMSRD ARL CS IS T 2800 POWDER MILL RD ADELPHI MD 20783-1197

NO. OF COPIES	ORGANIZATION
	ABERDEEN PROVING GROUND
1	DIR USARL AMSRD ARL CI OK TP (BLDG 4600)

NO. OF COPIES	ORGANIZATION
1	ARROW TECH ASSOCIATES W HATHAWAY 1233 SHELBURNE RD D-8 SOUTH BURLINGTON VT 05403
1	OREGON STATE UNIVERSITY DEPT OF MECHANICAL ENGRNG M COSTELLO CORVALLIS OR 97331
1	ATK R DOHRN MN07-LW54 4700 NATHAN LANE N PLYMOUTH MN 55442
1	AEROPREDICTION INC F MOORE 9449 GROVER DR STE 201 KING GEORGE VA 22485
1	ARDEC AMSTR AR FSF X W TOLEDO BLDG 95 SOUTH PICATINNY ARSENAL NJ 07806-5000

NO. OF COPIES	ORGANIZATION
	ABERDEEN PROVING GROUND
22	DIR USARL AMSRD ARL WM BC M BUNDY J DESPIRITO G COOPER J GARNER B GUIDOS K HEAVEY J NEWILL P PLOSTINS J SAHU S SILTON D WEBB P WEINACHT (5 CPS) A ZIELINSKI AMSRD ARL WM BD B FORCH AMSRD ARL WM BF S WILKERSON AMSRD ARL WM BA D LYON T BROWN AMSRD ARL WM B A HORST